# Seismic collapse of self-centering steel MRFs with different column base structural properties

**Vasileios C. Kamperidis**[a1], **Georgios S. Papavasileiou**[b], **George S. Kamaris**[c] **and George Vasdravellis**[d]

[a]School of Applied Sciences, Abertay University, Bell Street, Dundee, DD1 1HG, UK

[b]School of Architecture and Built Environment, University of Wolverhampton, Wulfruna Street, Wolverhampton, WV1 1LY, UK

[c]Department of Civil Engineering, Liverpool John Moores University, Liverpool, L3 3AF, UK

[d]Institute for Infrastructure and Environment, Heriot-Watt University, Edinburgh, EH14 4AS, UK

## ABSTRACT

The effect of the strength and stiffness characteristics of a previously proposed novel column base on the seismic performance and collapse capacity of steel self-centering moment-resisting frames is evaluated in this paper. This is done through three normalised parameters that represent the initial stiffness, post-yield stiffness, and strength of the column base, which can be independently adjusted. For these evaluations, a prototype steel building, which serves as a case study, is designed with sixteen different cases of a self-centering moment-resisting frame with different column base stiffness and strength characteristics (SC-MRF-CBs). A self-centering moment-resisting frame with conventional column bases and the same members and beam-column connections as those of the SC-MRF-CBs, named SC-MRF, serves as a benchmark frame. A set of 44 ground motions was used to conduct non-linear dynamic analyses and evaluate the seismic performance of the frames. Incremental dynamic analyses were also performed with the same ground motions set to evaluate the collapse capacity of the frames. Collapse capacity fragility curves and adjusted collapse margin ratios of the frames were derived and used for the comparison of the seismic risk of the frames. The

---

[1] Corresponding author, E-mail address: Vasileios.C.Kamperidis@gmail.com, ORCID ID number: 0000-0003-4893-7110.

results show that the new self-centering column base significantly improves the seismic performance of the SC-MRF, demonstrating the potential of the SC-MRF-CBs to be redesigned with smaller member sections. Moreover, the SC-MRF-CBs achieve significant reduction in collapse risk compared to the SC-MRF. Finally, the results show that increasing the base strength and stiffness improves the seismic performance and collapse capacity of the SC-MRF-CBs.

**KEYWORDS**

Column base; Self-centering; Collapse risk; Interstorey drifts and floor accelerations; Parametric investigation; Seismic resilience

# 1 INTRODUCTION

Column bases have a very important role in the seismic response of steel moment-resisting frames (MRFs) [1–5]. Eurocode 8 (EC8) [6] assumes that plastic hinges at the column base connection will offer increased rotational ductility compared to other plasticity mechanisms therein [7], such as column member plastic hinging. This strength-related code presumption has been questioned by Lignos and Krawinkler [8], who showed that the ductility of the column base plastic hinges may be compromised by local instabilities, leading to premature column failure. Moreover, Aviram et al. [5] and Ruiz-García and Kanvinde [3] showed that decreasing the initial stiffness of the base connections in low-rise buildings can change the height-wise drift distribution, leading to drift and damage concertation and eventually to collapse. Zareian and Kanvinde [2] showed that reducing the base fixity in low- to high-rise buildings can increase the members’ force demands, alter the global plastic mechanism, and significantly reduce ductility, strength and collapse resistance. Torres-Rodas et al. [4] showed that increasing the base flexibility of three-dimensional framed buildings, increases their transient drifts and probabilities of collapse, while appreciably decreases their overstrength and ductility.

To address the deficiencies of MRFs under earthquakes, the self-centering MRFs (SC-MRFs) were developed, such as those, for example, proposed in [9–16]. The main practice for SC-MRFs is to use post-tensioned (PT) beam-column connections that utilise high-strength steel tendons to clamp the beams to the columns and, thus, provide a re-centering mechanism that can restore the initial geometry of the building up to a targeted seismic intensity. High-strength steel is used to ensure that the tendons remain elastic up to the targeted frame response. Therefore, in these SC-MRFs, the self-centering mechanism is provided through attaining a targeted elastic elongation capacity for their PT tendons. Other researchers [17,18] have provided self-centering mechanisms for their seismic-resilient MRFs by relying on fully recoverable plastic deformations for the self-centering components of their systems up to as targeted response level to eliminate the need for repair, i.e., by utilising superelastic shape memory alloys (SMAs) for their self-centering components. The SC-MRFs with high-strength PT tendons, which are of interest in this work, utilise energy dissipating devices (EDs) in their PT beam-column connections to dissipate seismic energy and reduce the seismic forces and accelerations [9]. These EDs can be easily removed or replaced, if damaged, which can improve building's resilience [19,20]. Combining these techniques, SC-MRFs can minimize damage and residual drifts [10] and reduce peak drifts and floor accelerations [9,21].

Self-centering systems can offer an option of tuning the structural properties that fully define their seismic hysteretic response. These properties are the initial stiffness, post-yield stiffness, strength and energy dissipation. Different researchers have evaluated the effect of these properties on the seismic response of different types of self-centering systems. Christopoulos et al. [22,23] concluded that if adequate energy dissipation is provided in SDOF flag-shaped response systems, these could have similar or improved peak drift response compared to that of elastoplastic systems of the same initial stiffness and strength. It was highlighted, though, that systems with self-centering response are prone to increased resonance vibration amplitudes when their post-yield stiffness ratio, $\alpha$ (i.e., the ratio of the post-yield stiffness over the initial stiffness), is increased [23]. Subsequently, Christopoulos et al. [24] found that the maximum drift response of SDOF systems with self-centering response under the design basis earthquake (DBE) [6] slightly decreases for increasing values of their post-yield stiffness. Interestingly, this effect was reversed for the collapse prevention seismic performance level – a finding fundamentally opposite to what applies in elastoplastic systems. Karavasilis and Seo [25] concluded that increasing the strength and adding damping in self-centering SDOF systems, generally decreases their peak total accelerations and displacements. In contrast, Cimellaro [26] suggested that the drift response of a structure may be improved by adopting lower lateral strength combined with higher damping ratios. Chou and Chen [27] investigated the performance of SC-MRFs with either fixed or self-centering column bases under the DBE and maximum considered earthquake (MCE) [28]. However, they did not assess the effect of the base strength, stiffness and energy dissipation on the seismic response of their investigated systems.

SC-MRFs with conventional column bases still cannot fully avoid structural damage and residual drifts because of the plastic hinges developed at their column bases [9,10,27,29]. To address this issue, SC-MRFs with self-centering column bases with replaceable/repairable EDs (SC-MRF-CBs) were developed [27,29–33]. SC-MRF-CBs can eliminate damage at their column bases and, thus, exhibit negligible residual drifts. Kamperidis et al. [29] have shown that these systems significantly reduce the peak drifts compared to their correspondent SC-MRFs, i.e., the frame with the same PT beam-column connections and same members with the SC-MRF-CB, but with conventional rigid and full-strength column bases. In addition, the design procedure proposed in [29] has the ability to fine-tune in a controlled manner the strength, stiffness and hysteretic behaviour of a SC-MRF-CB, keeping these parameters uncoupled. Thus, one can design an SC-MRF-CB adjusting these parameters in such a way that its seismic response can be enhanced. However, an extensive and thorough parametric study on the effects of these parameters to the seismic response of the SC-MRF-CBs is still missing.

Moreover, the performance-based design approach of modern structural codes [28,34] mandates that buildings should be assessed against collapse as an extra measure of safety for human life, on the top of satisfying the traditional force and displacement requirements of the structural codes (e.g., EC8 [6]). This triggered research towards the collapse assessment of self-centering systems. In line with this, Tzimas et al. [35] found that the collapse capacity of SC-MRFs subjected to both far- and near-fault earthquakes, can be significantly improved by adding viscous dampers. However, the collapse risk of the SC-MRF-CBs and their potential to improve the collapse capacity of seismic-resistant steel buildings has never been evaluated.

This paper investigates the potential of SC-MRF-CBs equipped with the novel column base proposed in the work of Kamperidis et al. [29] to further improve the seismic performance and reduce the collapse risk of earthquake-resilient steel buildings equipped with SC-MRFs. The collapse risk of these new systems has never been assessed before and, so, it is of particular importance to investigate whether they attain a better or worse collapse behaviour compared to the SC-MRF. By comparing both the seismic performance and collapse risk of the SC-MRF-CBs with those of the SC-MRF, the performance of the former can be evaluated against all the performance criteria modern structural codes demand. As such, it can be concluded whether the SC-MRF-CBs can provide the potential to be designed for smaller steel members as compared to those of the SC-MRF. However, the explicit consideration of an SC-MRF-CB system with smaller cross-section than those of the SC-MRF is out of the scope of this work. Moreover, the mainstream approach for the SC-MRFs is to be designed for similar strength and initial stiffness with their correspondent conventional MRF [10,36], referred to as correspondent MRF. Besides, due to the specific configuration of their PT beam-column connections, SC-MRFs do not allow for flexible stiffness and strength frame adjustments. For that reason, SC-MRFs are rather restricted to adhere to the above design approach. In contrast, the self-centering column bases allow for the controlled adjustment of all the structural properties that are necessary to fully determine their hysteretic behaviour to targeted predefined levels through mathematical formulas [29]. This base structural properties' control mechanism enables the adjustment of the stiffness and strength of the SC-MRF-CBs. An enhanced design procedure (compared to that in [29]) for the self-centering column bases is also proposed. This work thoroughly and methodologically investigates for the first time the effects of all the aforementioned base structural properties on the seismic performance and collapse capacity of the SC-MRF-CBs for a given level of energy dissipation in their bases. The base structural properties in question are the initial stiffness, post-yield stiffness, and strength, represented through three normalised factors, which are described next (Section 3.1). For this scope, a prototype steel building was designed that comprises different seismic-resistant frames: i.e., an SC-MRF and sixteen SC-MRF-CBs with different base stiffness and strength characteristics. The frames were modelled in OpenSees, where material and geometrical nonlinearities were taken into account, along with strength and stiffness degradation. A set of 44 ground motions, scaled to three code-prescribed seismic intensity levels [6,28], was used to conduct dynamic analyses and evaluate the seismic performance of the frames. In addition, incremental dynamic analyses (IDAs) were performed with the same set of ground motions to evaluate the collapse capacity of the frames. The collapse capacity fragility curves and the adjusted collapse margin ratio of the frames were derived and used for the comparison of the seismic risk of the frames.

## 2 PROTOTYPE BUILDING

The 5- by 3-bay, five-storey prototype steel building of [29], depicted in Figure 1, is utilised in this work. Figure 1 shows the two identical braced frames in the *Y* direction and two identical seismic-resistant frames in the *X* direction the building has at its perimeter. The building has ductile non-structural elements and thus, the maximum interstorey drift ratio, $\theta_{s,max}$, must be less than 0.75% under the frequent occurred earthquake (FOE) in accordance with EC8 [6]. The design spectrum of EC8 [6] with peak ground acceleration equal to 0.35g and ground type B was used for the design of the frame under the DBE.

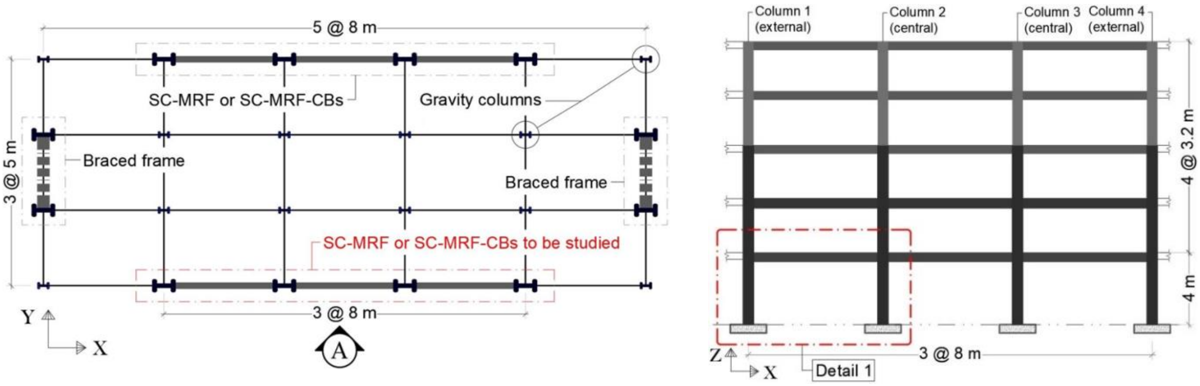

(a) (b)

Figure 1 (a) Plan view; and (b) Elevation A of the prototype building.

Only the seismic-resistant frame of Elevation A of the prototype building, shown in Figure 1(b), is studied in this work. The frame of interest was designed as: (a) an SC-MRF, following the design procedure of [10], to serve as the benchmark frame of this work; and (b) sixteen different SC-MRF-CBs with the self-centering column bases proposed in [29], having different base stiffness and strength characteristics but the same energy dissipation. The SC-MRF and all SC-MRF-CBs have the same beams, columns and PT beam-column connections. The design characteristics of the members and PT beam-column connections of the SC-MRF are those described in [35]. Figure 2(a) illustrates the bottom-left part of an SC-MRF-CB in Elevation A of the prototype building. The configurations of an external and internal (central) PT beam-column connection of the frames are depicted in Figure 2(a). Figure 2(b) shows a close-up view and the notation of these connections. The design procedure proposed in [29] was used for the design of the self-centering column bases of the SC-MRF-CBs.

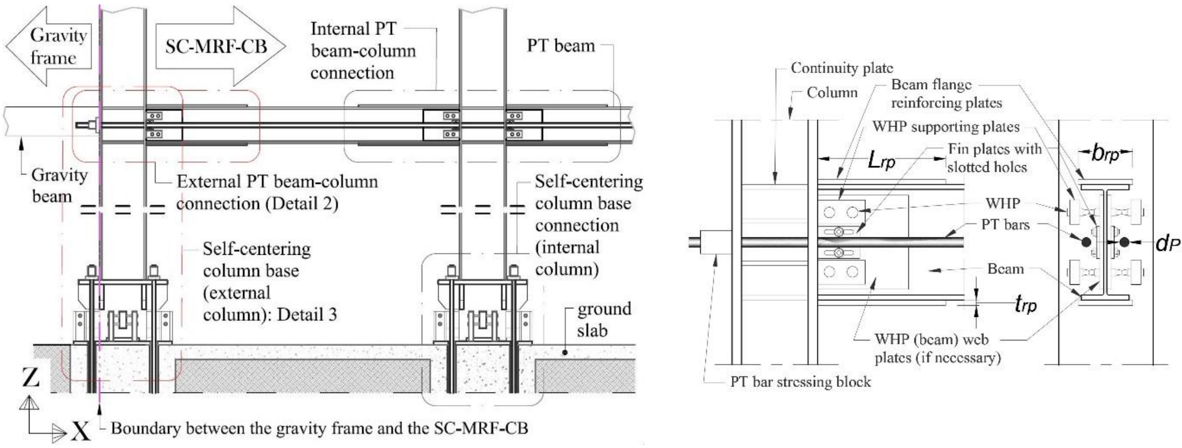

(a) (b)

Figure 2 Close-up view of: (a) the bottom-left part of the SC-MRF-CB in Elevation A of the prototype building (Detail 1 in Figure 1(b)); and (b) PT beam-column connection at an external column with its notation (Detail 2 in Figure 2(a)).

The web hourglass pins (WHPs) described in [13] were utilised as EDs in the column bases of the SC-MRF-CBs. The material of the WHPs was duplex stainless steel and its properties were as follows, as per [14]: yield stress equal to 543 MPa; ultimate stress equal to 778 MPa; elongation at fracture 34.25%; and Young’s modulus equal to 227.848 GPa. The material for the multi-wire tendons of the self-centering column bases was the low-relaxation Grade 270 steel material of ASTM A416 [37] with yield strength of 1676 MPa; ultimate tensile strength of 1860 MPa; Young’s modulus equal to 195 GPa; and ultimate elongation 3.5%. This material, used in [38] and [39], is utilised in Section **Error! Reference source not found.** for the fracture modelling of the tendons.

## 3 DESIGN CASES

Sixteen SC-MRF-CB design cases with different values for the strength, initial stiffness, and post-yield stiffness of their self-centering column bases are employed for the parametric study of this work. Thus, each self-centering column base employs a unique combination of values for these three base structural properties. There are three values of strength, three values of initial stiffness and five values of post-yield stiffness that are combined to form these sixteen combinations in the self-centering column bases. These values cover the whole range of feasible values that can be achieved each base structural property when designing the self-centering column utilising the design procedure proposed in [29]. The three ranges of feasible values of the base structural properties are delimited by the given column cross-section and column design loads, which serve as input for the aforementioned design procedure [29]. The column and its design loads are derived from the elastic analysis and design of the correspondent MRF, from which the SC-MRF-CBs' designs stem [29]; this will be further explained next (Section 3.2). By examining self-centering column bases with base structural properties that span the whole range of their feasible values, the limits of the distinct effect of each one of these properties on the seismic response and collapse capacity of the SC-MRF-CBs can effectively be determined. The notation of the self-centering column bases can be seen in Figure 3(a). Each self-centering column base is considered to be a cantilevered assembly that comprises the self-centering low-damage column base connection, proposed in [29], and the steel column member of the first storey of the frame (Figure 3(a)). The self-centering column base connections are determined by the height of the concrete-filled tube (CFT) (seen in Figure 3(a)), $L_{CFT}$. The steel columns extend from the top of their self-centering base connections up to the lower limit of the panel zones of the first-storey PT beam-column connections. This limit is the level of the bottom flanges of the first-storey PT beams, as indicated by the red dashed line in Figure 3(a). The steel columns are determined by their length, $L_c$, as it is shown in Figure 3(a).

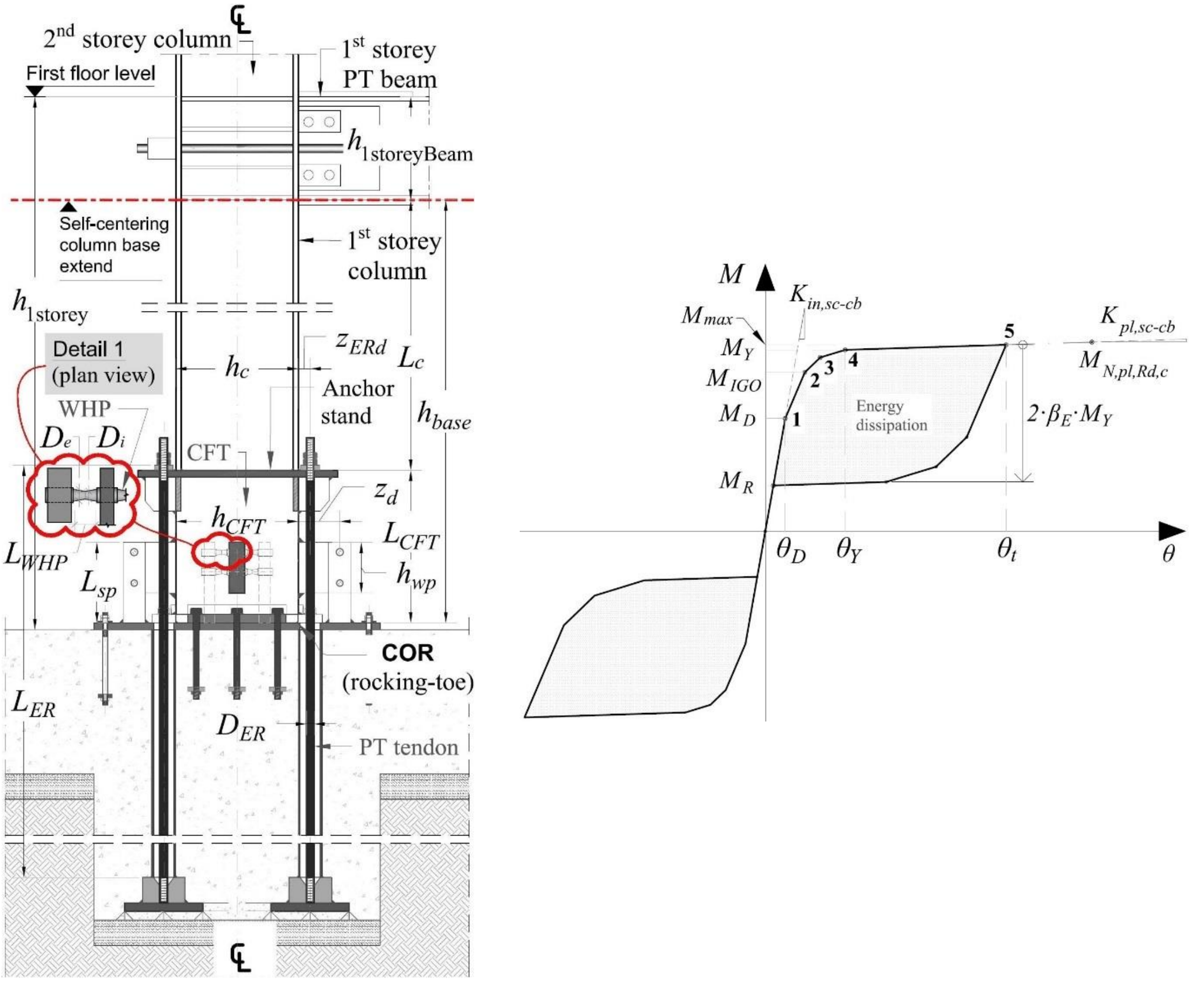

(a) (b)

Figure 3 Self-centering column base: (a) configuration (Detail 3 in Figure 2(a)) and notation; and (b) theoretical moment ($M$)-rotation ($\theta$) behaviour for an assumed clockwise bending moment and axial force.

The rationale for considering this specific cantilevered assembly configuration as the means of assessing the base stiffness and strength of the SC-MRF-CBs is that it exclusively includes the only two elements that change in the whole configuration of the SC-MRF-CBs, i.e., the base connection and its connecting steel first-storey column. All the other parts of the frames are the same as those of the SC-MRF. Similar approaches have been adopted in previous relevant research [40]. Such an approach facilitates the large computational demands of this work. The theoretical moment ($M$)-rotation ($\theta$) behaviour of the self-centering column bases can be seen in Figure 3(b). In this figure, $\theta$ is the chord rotation of the self-centering column bases, defined as the lateral displacement at the top of the column divided by the total height of the column bases, $h_{base}$. Thus, $h_{base}$ is related with the geometry of the frame through the following relation:

$$h_{base} = h_{1storey} - h_{1storeyBeam} \quad (1)$$

where $h_{1storey}$ is the total height of the first storey and $h_{1storeyBeam}$ is the cross-sectional depth of the beams of the first floor.

### *3.1 Investigated base structural properties*

The investigated structural properties of the self-centering column bases (or simply base structural properties) that are studied in this work are their strength, $M_{IGO}$, initial stiffness, $K_{in,sc\text{-}cb}$, and post-yield stiffness, $K_{pl,sc\text{-}cb}$, which are described in Figure 3(b). $M_{IGO}$ is the moment at the first yielding of the WHPs of the self-centering column base connection (Figure 3(b)). $M_{IGO}$ is considered to represent the flexural strength of the self-centering column bases because the strength of a system with metallic fuses should correspond to the point where the first yielding of its structural fuses occurs [41]. The self-centering column base allows the controlled adjustment of these base structural properties by utilising the analytical expressions that are presented next. To uncouple the research findings of this work from the specific design characteristics of the frames studied herein (e.g., the size of the first-storey columns, the cross-sectional depth of which, denoted as $h_c$ (see Figure 3(a)), and its plastic moment of resistance, $M_{N,pl,Rd,c}$ (described in Eq. (3), below), are of interest in this study), the base structural properties are represented by the following normalised parameters: (a) the strength ratio, $\eta$; (b) the normalised initial base stiffness factor, $\beta_{base}$; and (c) the post-yield stiffness ratio, $\alpha$. Thus, the findings of this work can be extended to any SC-MRF-CB that is designed as per the design procedure proposed in [29].

Likewise previous research [25,42], the energy dissipation factor, $\beta_E$, is utilised to control the energy dissipation in all sixteen self-centering column bases. $\beta_E$ was selected to take the same, near-maximum allowable value to allow the self-centering behaviour of the column bases and maximise their seismic energy dissipation. Thus, $\beta_E$ was not included in the parametric study. Based on previous relevant research [22,23,43], it was hypothesized that by maximising the energy dissipation at the column bases, the seismic response and collapse capacity of the SC-MRF-CBs would be optimally improved. Because the upper bound of $\beta_E$ equals 0.5 [25,42], $\beta_E$ was conservatively taken equal to 0.48 in all self-centering column bases. The energy dissipation in each self-centering column base is due to the energy dissipated by the WHPs up to the target base rotation, $\theta_t$ (Figure 3(b)); the steel columns were intended to remain elastic and not contribute to the energy dissipation of the self-centering column bases. For this research, $\theta_t$ was conservatively chosen to be equal to the rotation capacity limit of EC8 for ductility class high MRFs, i.e., 0.035 radians [6]. This implies that no strength and stiffness deterioration was expected to take place up to $\theta_t$. $\beta_E$ was defined as:

$$\beta_{\mathrm{E}} = \frac{M_Y - M_D}{M_Y} \tag{2}$$

where $M_Y$ is the moment of the self-centering column bases when all WHPs have reached their elastic limit; and $M_D$ is the decompression moment of the self-centering connection, i.e., the moment at which the gap at the rocking interface of the column base opens [10,29]. These characteristic moments, along with their corresponding rotations, can be seen in Figure 3(b).

The strength factor, $\eta$, was defined as:

$$\eta = \frac{M_{IGO}}{M_{N,pl,Rd,c}} \tag{3}$$

where $M_{IGO}$ is the moment at the first yielding of the WHPs of the self-centering column base connection; $M_{N,pl,Rd,c}$ is the plastic moment of resistance of the column. $M_{N,pl,Rd,c}$ accounts for interaction with the design axial force, $N_{Ed}$, and the overstrength of the connections materials and for other material effects, in accordance with EC8 [6] and Eurocode 3 (EC3) [44] provisions. $N_{Ed}$ is the axial force derived from the analysis of the correspondent MRF for the gravity loads combination of actions [29]. The strength factor $\eta$ consists a measure of the strength of the base connection but can represent the strength of the whole self-centering column base because the former is the only part of the latter that is expected to yield up to $\theta_t$. The concept that the strength factor $\eta$ consists a measure of the column bases' strength was adopted on the basis that it relates the yield strength of the base connections with that of the column member. This is in line with the relevant provisions of Eurocode 3 [45] that classify moment-resisting connections with respect to their strength by comparing the strength of the connections with the strength of their connecting members. Previous research on PT beam-column connections [10] has set out an upper limit for $\eta$ equal to unity. The parametric investigation of this work shown that to achieve self-centering and damage-control behaviour up to $\theta_t$, only values of $\eta$ below 0.45 were capable of yielding self-centering column base designs with initial and post-yield stiffness within their feasible range of values; these latter two base structural properties were controlled through their normalised factors, $\beta_{base}$ and $\alpha$, respectively, described next. For that reason, the three values of $\eta$ this work examined were 0.30, 0.35 and 0.40.

The normalised initial base stiffness factor, $\beta_{base}$, was defined as:

$$\beta_{base} = \frac{K_{in,sc-cb}}{K_{in,conv}} \tag{4}$$

where $K_{in,conv}$ is the initial (elastic) flexural stiffness of a cantilever-fixed steel column of total height equal to $h_{base}$; and $K_{in,sc\text{-}cb}$ the initial stiffness of a self-centering column base, assumed equal to the elastic flexural stiffness of the steel cantilevered column on the top of the self-centering column base connection, $K_{el,col}$, since the initial stiffness of the latter connection is taken as infinite [29]. Thus, $K_{el,col}$ is calculated for a column height of $L_c$. For the self-centering column bases under investigation, the three $\beta_{base}$ values examined were 133%, 167% and 200%.

The post-yield stiffness ratio, $\alpha$, was defined according to the following relation:

$$\alpha = \frac{K_{pl,sc-cb}}{K_{in,sc-cb}} \tag{5}$$

where $K_{pl,sc\text{-}cb}$ is the post-yield stiffness of the self-centering column base, defined as:

$$K_{pl,Sc-Bc} = \frac{K_{pl,sc-cb} \cdot K_{el,col}}{K_{pl,sc-cb} + K_{el,col}} \tag{6}$$

where $K_{pl,sc\text{-}cb}$ is the post-yield stiffness of the self-centering column base connection, which was determined by the following relation [29]:

$$K_{pl,sc-cb} = K_{fe} \cdot \left(\lambda \cdot n_{WHPu} \cdot z_u^2 + \lambda \cdot n_{WHPc} \cdot z_c^2 + \lambda \cdot n_{WHPd} \cdot z_d^2\right) + K_{ER} \cdot \left(n_{ERu} \cdot z_{ERu}^2 + n_{ERd} \cdot z_{ERd}^2\right) \tag{7}$$

where $k_{fe}$ is the elastic stiffness of a single WHP [29]; $\lambda$ equals 2% according to [29]; $n_{WHPu}$ and $n_{WHPd}$ are the numbers of the WHPs at the gap-opening and rocking-toe side of the self-centering column base connections (the rocking toe coincides with the centre of rotation of the connection (COR), as it is seen in Figure 3(a) for an assumed clockwise moment); $n_{WHPc}$ the number of the central WHPs; $z_u$, $z_d$ and $z_c$, the lever arms of the WHPs at the gap-opening side, rocking-toe side and that of the central WHPs, respectively; $K_{ER}$ is the elastic axial stiffness of each tendon, equal to $E_{ER} \cdot A_{ER}/L_{ER}$, with $E_{ER}$, $A_{ER}$ and $L_{ER}$ the tendon's material Young's modulus, cross-sectional area and length, respectively; and $n_{ERu}$ and $n_{ERd}$, and $z_{ERu}$ and $z_{ERd}$ the number and lever arms of the PT tendons at the gap-opening and rocking-toe side of the self-centering column base, respectively. The lever arms $z_d$ and $z_{ERd}$, are defined in Figure 3(a). The lever arms $z_u$ and $z_{ERu}$ were derived by adding to $z_d$ and $z_{ERd}$ the cross-sectional depth of the CFT, $h_{CFT}$, respectively. $z_c$ equals $h_{CFT}/2$. Five different values of $\alpha$ were examined in this work, i.e., 5%, 10%, 15%, 20% and 24.5%. The value of 24.5% was the maximum value of $\alpha$ obtained for the given level of strength and initial stiffness of the relevant self-centering column base. This is in agreement with the maximum achievable limit of $\alpha$ for real flag-shaped response systems, determined to about 25%, proposed by Wiebe and Christopoulos [46].

### *3.2 Self-centering column base design procedure*

This section presents the design procedure utilised to derive the sixteen self-centering column base designs that are investigated in this work. The design procedure is that described in the work of Kamperidis et al. [29], with the only difference being that – in this work – the investigated base structural properties are given pre-selected values utilising Eq. (2) through (7) of Section 3.1. Pre-selecting these values, reduces the number of unknowns to be determined (as compared to the approach adopted in [29]), significantly facilitating the design process. To minimize repetition since the design procedure in [29] has been presented therein in detail, the design approach adopted in this work presents only limited mathematical formulas from [29].

To initiate the design procedure, the following input quantities are required: the column axial force, $N_{Ed}$; the column cross-section, so that its cross-sectional depth, $h_c$, and plastic moment of resistance, $M_{N,plRd,c}$, are determined; and the target base rotation, $\theta_t$. The design procedure comprises the following steps:

Step 1: Design the tendons

(a) Select a value for $\beta_{base}$ and calculate $K_{in,sc\text{-}cb}$ from Eq. (4). From $K_{in,sc\text{-}cb}$, $L_c$ is derived utilising the relevant elastic flexural stiffness formula from mechanics (Section 3.1). From Figure 3(a) and given the resulted $L_c$ value, $h_{CFT}$ can be derived.

(b) Select a value for the strength factor, $\eta$. From Eq. (3) $M_{IGO}$ can then be derived.

(c) Select a value for the ratio $M_D/M_{IGO}$ so that is it larger than 0.5, but as closer as it gets to that latter value. This is to ensure self-centering capability but also to maximize energy dissipation. Thus, $M_D$ is derived.

(d) Select a number, $n_{ERu}$=$n_{ERd}$, and a lever arm for the tendons, e.g., $z_{ERd}$ ($z_{ERu}$ can be determined as per Section 3.1). It is suggested that four tendons are placed at the corners of the anchor stand, which is the elevated stiff plate welded on the top of the CFT (see Figure 3(a)); i.e., $n_{ERu}$=$n_{ERd}$=2. Then, calculate the initial post-tensioning force at each tendon, $T$, as per Eq. (2) of Kamperidis et al. [29].

(e) Select an appropriate high-strength steel grade material for the tendons, e.g., Grade 270 steel material of ASTM A416, to ensure a high yield strength, $f_{y,ER}$, for the tendons, and assume a diameter for them, $D_{ER}$ (this determines $A_{ER}$). Then, utilize Eq. (3) of [29] to calculate $L_{ER}$. Also, approximate the moment contribution of the tendons for the characteristic rotation, $\theta_2$, denoted as $M_{ER}(\theta_2)$, as per Eq. (7) of [29]. $\theta_2$ is the rotation at which the first WHP of the self-centering column base yields. $M_{ER}(\theta_2)$ is to be used next.

Step 2: Design the WHPs

(a) Select a number for the WHPs at each side of the self-centering column base (e.g., $n_{WHPd}$). It is suggested that two WHPs are placed at all sides of the column base; this is for construction practicality and to ensure that the column base control its structural properties over both of its main axes [29]; i.e., $n_{WHPd}$= $n_{WHPc}$= $n_{WHPu}$= 2. Also, select a lever arm for the WHPs, e.g., $z_d$ ($z_u$ and $z_c$ can be determined as per Section 3.1). Then, calculate the yield strength of a single WHP, $F_{y,WHPi}$, as per Eq. (5) of [29], utilising $M_{ER}(\theta_2)$ from Step 1(e). The internal diameter of the WHPs, $D_i$ (described in Detail 1 of Figure 3(a)), can then be calculated from the following relation as per [10,29]:

$$D_i = \sqrt{\frac{2 \cdot F_{y,WHP,i} \cdot \sqrt{3}}{\pi \cdot f_{y,WHP}}} \tag{8}$$

where $f_{y,WHP}$ is the yield strength of the material of the WHPs.

(b) Select a value for $\alpha$, and based on Eq. (5) and the value of $K_{in,sc\text{-}cb}$ derived from Step 1(a), calculate $K_{pl,sc\text{-}cb}$. Based on the $K_{pl,sc\text{-}cb}$ value, calculate the WHPs' elastic stiffness $K_{fe}$ from Eq. (7). Moreover, to derive a relationship between the length of the tapered part of half a WHP, $L_{WHP}$, and the external diameter of the WHP, $D_e$, substitute $D_i$ from Eq. (8) into the following relationship [29,47]:

$$L_{WHP} = \frac{2.566 \cdot D_e^3}{\pi \cdot D_i^2} \tag{9}$$

Both $L_{WHP}$ and $D_e$ are described in Detail 1 of Figure 3(a). A second relationship between $L_{WHP}$ and $D_e$, can be derived by substituting $K_{fe}$ from above and $D_i$ from Eq. (8) into the following relationship [13,29]:

$$K_{fe} = 2 \cdot \frac{9 \cdot \pi \cdot D_e^3 \cdot D_i \cdot E_{WHP} \cdot G_{WHP}}{40 \cdot E_{WHP} \cdot D_e^2 \cdot L_{WHP} + 48 \cdot G_{WHP} \cdot L_{WHP}^3} \tag{10}$$

where $E_{WHP}$ and $G_{WHP}$ are the elastic and shear moduli of the WHP material. Solving the system of Eqs. (9) and (10), the values of $D_e$ and $L_{WHP}$ can be derived.

Step 3: Check the self-centering capability of the column base and the column plastic hinge avoidance

The self-centering capability of the column bases is checked by utilising Relationships (9) through (11) and Relationship (17) from [29]. There are two cases:

(a) If self-centering behaviour is achieved, then proceed with checking whether a plastic hinge is formed at the bottom of the column member. This is done by utilising Relationship [20] of [29]. Two case are now identified:

1. A plastic hinge is formed: in this case, decrease $A_{ER}$ in Step 1(e) by be employing a smaller tendon (smaller $D_{ER}$), and repeat all steps up to this point until this check is satisfied. Then finalize the procedure.
2. A plastic hinge is not formed: in this case, finalize the design process.

(b) If self-centering behaviour is not achieved, return to Step 1(c) and increase the ratio $M_D/M_{IGO}$. Then, repeat the design procedure up to Step 3(a) until self-centering is achieved and plastic hinge is not formed at the column. When Step 3(a) is fully satisfied, complete the design process.

The design steps are summarized in the flowchart of Figure 4.

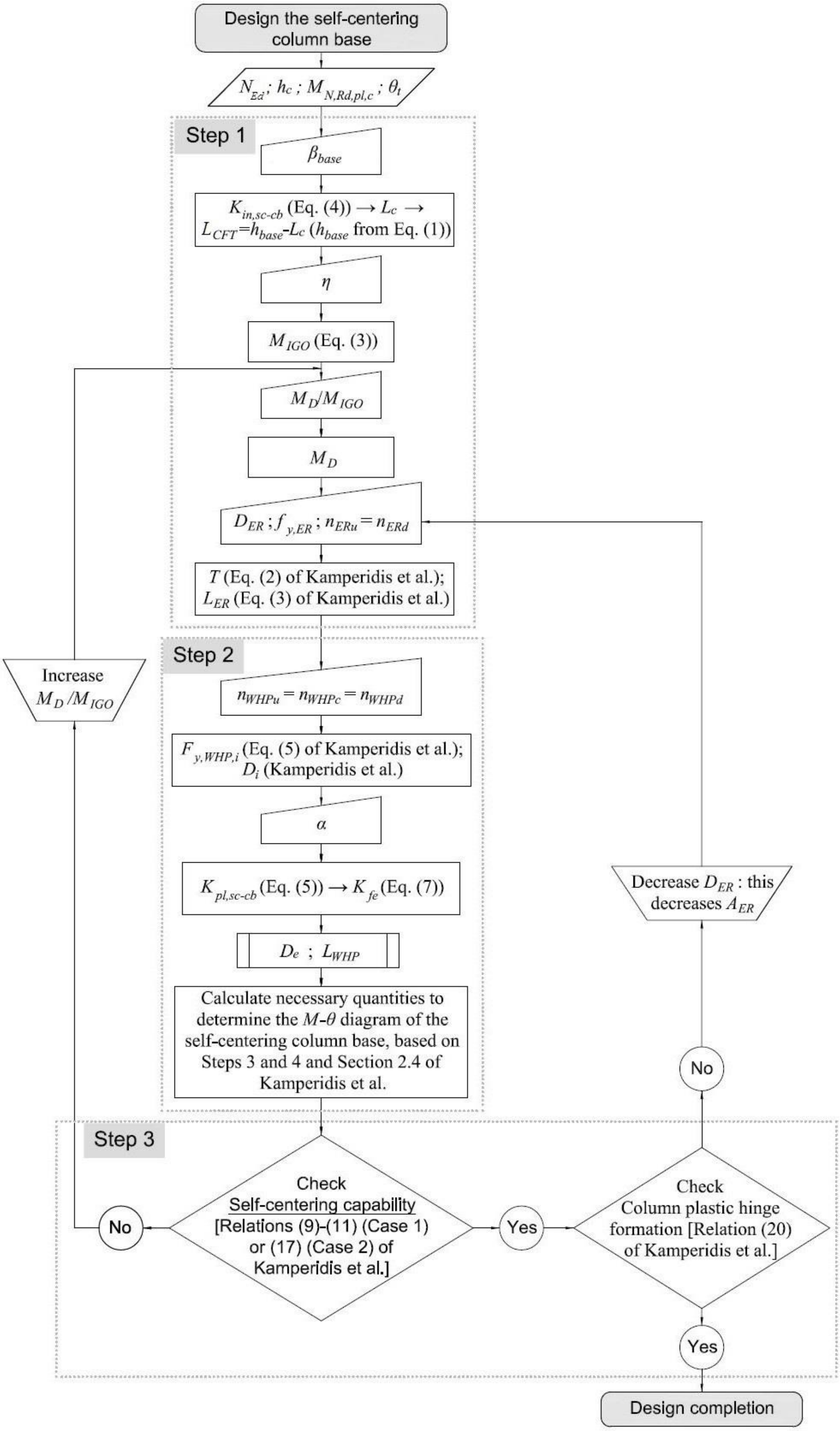

Figure 4 Flowchart of the design approach of the self-centering column bases, based on the design procedure proposed in Kamperidis et al. [29].

### *3.3 Self-centering column base designs*

Table 1 lists the normalised base structural properties of the sixteen self-centering column base designs and Table 2 presents their key design characteristics. These design characteristics were derived utilising the design procedure presented in Section 3.2. The notation utilised in Table 2 is described in Figure 3(a) (and its Detail 1) and in Section 3.2.

Table 1. Normalised base structural properties of the sixteen self-centering column bases.

| Frame | $\eta$ | $\beta_{base}$ (%) | $\alpha$ (%) |
|---|---|---|---|
| H40K133A5 | 0.4 | 133 | 5 |
| H40K133A15 | 0.4 | 133 | 15 |
| H40K167A15 | 0.4 | 167 | 15 |
| H40K167A5 | 0.4 | 167 | 5 |
| H40K133A10 | 0.4 | 133 | 10 |
| H40K167A10 | 0.4 | 167 | 10 |
| H40K133A24 | 0.4 | 133 | 24.5 |
| H35K133A5 | 0.35 | 133 | 5 |
| H35K133A15 | 0.35 | 133 | 15 |
| H35K167A15 | 0.35 | 167 | 15 |
| H35K167A5 | 0.35 | 167 | 5 |
| H35K133A10 | 0.35 | 133 | 10 |
| H35K167A10 | 0.35 | 167 | 10 |
| H35K200A10 | 0.35 | 200 | 10 |
| H35K133A20 | 0.35 | 133 | 20 |
| H30K133A10 | 0.30 | 133 | 10 |

Table 2. Key column base design characteristics of the sixteen SC-MRF-CBs.

| Frame | $L_{WHP}$ (m) | $D_e$ (m) | $D_i$ (m) | $F_{y,WHP,i}$ (kN) | $K_{fe}$ (MN/m) | $L_{sp}$ (m) | $h_{wp}$ (m) | $L_{ER}$ (m) | $D_{ER}$ (m) | $z_d$ (m) | $z_{ER,d}$ (m) | $L_{CFT}$ (m) | $T$ (kN) |
|---|---|---|---|---|---|---|---|---|---|---|---|---|---|
| H40K133A5 | 0.12 | 0.04 | 0.02 | 161.78 | 109.22 | 0.37 | 0.24 | 7.49 | 0.02 | 0.24 | 0.09 | 0.44 | 262.70 |
| H40K133A15 | 0.07 | 0.03 | 0.02 | 156.39 | 260.19 | 0.33 | 0.21 | 7.47 | 0.02 | 0.26 | 0.16 | 0.44 | 271.41 |
| H40K167A15 | 0.06 | 0.03 | 0.02 | 158.54 | 307.41 | 0.33 | 0.20 | 7.39 | 0.02 | 0.24 | 0.37 | 0.73 | 273.25 |
| H40K167A5 | 0.21 | 0.05 | 0.02 | 151.38 | 38.68 | 0.40 | 0.27 | 9.59 | 0.02 | 0.25 | 0.38 | 0.73 | 228.89 |
| H40K133A10 | 0.06 | 0.04 | 0.02 | 166.28 | 357.10 | 0.33 | 0.20 | 8.50 | 0.02 | 0.21 | 0.15 | 0.44 | 274.02 |
| H40K167A10 | 0.10 | 0.04 | 0.02 | 132.46 | 122.24 | 0.34 | 0.22 | 7.62 | 0.02 | 0.42 | 0.37 | 0.73 | 261.05 |
| H40K133A24 | 0.06 | 0.03 | 0.02 | 163.63 | 396.73 | 0.32 | 0.20 | 5.52 | 0.03 | 0.19 | 0.10 | 0.44 | 281.83 |
| H35K133A5 | 0.12 | 0.04 | 0.02 | 136.90 | 89.09 | 0.36 | 0.23 | 7.58 | 0.02 | 0.27 | 0.12 | 0.44 | 204.77 |
| H35K133A15 | 0.06 | 0.04 | 0.02 | 142.89 | 264.52 | 0.32 | 0.20 | 6.64 | 0.02 | 0.22 | 0.16 | 0.44 | 212.16 |
| H35K167A15 | 0.06 | 0.03 | 0.02 | 100.44 | 189.61 | 0.30 | 0.18 | 7.32 | 0.02 | 0.56 | 0.36 | 0.73 | 212.51 |
| H35K167A5 | 0.19 | 0.04 | 0.02 | 125.10 | 34.27 | 0.38 | 0.26 | 8.73 | 0.02 | 0.27 | 0.38 | 0.73 | 171.44 |
| H35K133A10 | 0.08 | 0.04 | 0.02 | 142.58 | 184.52 | 0.34 | 0.21 | 6.35 | 0.02 | 0.23 | 0.16 | 0.44 | 207.34 |
| H35K167A10 | 0.05 | 0.04 | 0.02 | 88.76 | 184.92 | 0.30 | 0.17 | 8.65 | 0.02 | 0.70 | 0.36 | 0.73 | 215.25 |
| H35K200A10 | 0.06 | 0.04 | 0.02 | 125.24 | 251.67 | 0.31 | 0.19 | 8.70 | 0.02 | 0.34 | 0.50 | 0.91 | 212.51 |
| H35K133A20 | 0.06 | 0.03 | 0.02 | 113.55 | 252.32 | 0.31 | 0.18 | 7.64 | 0.03 | 0.44 | 0.13 | 0.44 | 212.51 |
| H30K133A10 | 0.06 | 0.03 | 0.02 | 104.64 | 212.41 | 0.30 | 0.18 | 5.99 | 0.03 | 0.37 | 0.15 | 0.44 | 151.00 |

## 4 NON-LINEAR MODELS

The OpenSees platform [48] was used to model the prototype SC-MRF and SC-MRF-CBs. The PT beam-column connections in all frames were modelled as in [35]. The columns and the length of the beams that is reinforced were modelled with beam-column fiber elements that exhibit bi-linear elastoplastic stress-strain behaviour. Force-based beam-column fiber elements with end hinges [49] were used for the un-reinforced lengths of the beams. The stress-strain cyclic behaviour of the fibers was modelled by utilising the modified Ibarra-Krawinkler model [50]. This model was used because it captures the strength and stiffness degradation resulting from beam local buckling observed after the end of the beam flange reinforcing plates. This type of modelling was used in [51] and results in hysteretic curves for flexural members that are smooth and similar to the ones observed in experiments. The Ibarra-Krawinkler model does not take into account the effect of a variable axial force on the bending deterioration parameters [51]. The use of fiber elements results in reductions of the bending strength of the beam-column elements due to the variable axial-moment interaction [51]. Thus, this approach also captures the axial force (caused by the PT force at the tendons) – bending moment interaction in the beams of the frames [35,51]. Panel zones are modelled based on [52]. The OpenSees model developed in [29] is used for the column bases of the SC-MRF-CBs. The gravity columns of the tributary area of the frames are modelled as three lean-on columns to take into account P-Δ effects. Truss elements that connect the nodes of the lean-on columns to nodes defined along the length of the beams at the points where the secondary beams are placed are used to model diaphragm action of the composite slabs. The diaphragm also helps to avoid the shortening of the PT beams (as these are seen in Figure 2(a)) due to the increase of the post-tensioning forces caused by to the connections' gap opening and closing during seismic loads (the PT beams are only resist the constant axial force caused by the initial post-tensioning of their PT bars [10]). The stiffness of these trusses is 100 times larger than that of the axial stiffness of the beam. By connecting separately each bay's secondary beam nodes with the corresponding lean-on column node of the same storey, these stiff truss elements help to model the discontinuity between the composite slabs that correspond to each different bay of the self-centering system, as per the tributary area of the bay. Discontinuity between the composite slab and the flanges of the columns of the self-centering system is also assumed for the floor system utilised in this work [53]. The aim of the above floor system discontinuities is to avoid that the PT beam be restrained by the composite slab (minimizing the damage in the slab also); allow the free gap opening and closing of the PT connection (thus, not affecting the connection's hysteretic behaviour) [10,53]; and allow for the unobstructed self-centering frame expansion [10,36]. More details on the adopted floor system can be found in [10,53,54]. The tendons of the column bases were modelled to fracture to more accurately simulate the actual collapse limit of the frames under investigation. To this purpose, the Fatigue material of OpenSees [48] was utilised in conjunction with the parent material of the tendons. The parent material of the tendons is the material around which the Fatigue material is wrapped [48], and which in this case is the material steel01 of OpenSees [48]. The material steel01 has a bilinear elastoplastic hysteresis with post-stiffness ratio equal to 0.03 [29]. The Fatigue material is wrapped around the steel01 material without altering the stress-strain relationship of the latter [48]. The Fatigue material utilises the Coffin-Manson relationship [55] and the Palmgren-Miner linear damage accumulation rule [55] to model their low-cycle fatigue and fracture. The Coffin-Manson rule is expressed by the relationship:

$$\frac{\Delta\varepsilon_p}{2} = \varepsilon_f' \cdot \left(2 \cdot N_f\right)^m \tag{11}$$

where $\frac{\Delta\varepsilon_p}{2}$ is the plastic strain amplitude; $\varepsilon_f'$ the fatigue ductility coefficient, which represents the intersect of the plastic asymptotic line of the Coffin-Manson curve in the log-log space, i.e., the strain at which one cycle will cause failure (fracture) [55,56]; $N_f$ the number of the full cycles to failure (or $2 \cdot N_f$ the number of load reversals to failure); and $m$ the fatigue ductility exponent, which represents the sensitivity of the log of the strain amplitude to the log of $N_f$ [56], i.e., the slope of the Coffin-Manson curve in the log-log space. For the Fatigue material of the tendons, $\varepsilon_f'$ was taken equal to 4%. This strain value is a conservative fracture value as: (a) it represents the initial wire fracture of the strands of the tendons, ignoring the appreciable strength reserve that remains at the tendons afterwards and through the fracture of all their wires [38,39]; (b) it considers the premature fracture of the tendons due to excessive stress concentration at the vicinity of their anchors, as per the work of Bruce and Eatherton [38], where the fracture value in question represents the average observed first-wire fracture limit (not the relevant proposed design limit) from their tested specimens, considering both the tendon materials used therein, and also a newer multiple-use barrel and wedge anchorage system that allowed for larger inelastic strains prior to initial wire fracture, compared to the traditional barrel and wedge anchorage system that the authors also tested in their work; (c) it represents the upper first-wire fracture limit attained from the tested specimens in the work of Sideris et al. [39], given that their observed strain fracture values ranged from 1.5% to 4%; and (d) it is a value much smaller than those provided by these tendons manufacturers, i.e., 6-7% [57]. The fatigue ductility exponent, $m$, for the Fatigue material of OpenSees, was taken equal to -0.458, as per the work of Uriz [56]. For the maximum values of strain to be set out in the model of the material, the suggested minimum and maximum values of -1e16 and 1e16, respectively, have been adopted [48]. To accumulate damage in the material due to the random strain amplitude excursions during an earthquake, the Fatigue material of OpenSees utilises a rainflow method [55] counting algorithm to count the number of cycles at various strain amplitudes, in conjunction with the

Palmgren-Miner's linear damage accumulation Rule [55]. The Palmgren-Miner's Rule is expressed by the damage index, $D$, which is given by the following mathematical formula:

$$D = \sum_{i=1}^{j} \frac{n_i}{N_{f,i}} \tag{12}$$

where $N_{f,i}$ is the number of cycles that can be resisted by the material until failure at the $i$th constant strain amplitude loading, in a total of $j$ such loadings with constant strain amplitudes; and $n_i$ is the number of loading cycles the material has undergone at the $i$th constant strain amplitude loading [55]. Once index $D$ in the Fatigue material reaches the value of 1.0, the force (or stress) in the parent material becomes zero, signalling the failure of the parent material [48].

The fracture of the WHPs was not modelled in this study, as, based on previous experimental and numerical studies [14,54,58], their geometry and position around the column bases can be selected to avoid fracture before the building's seismic collapse due to second order effects [51].

# 5 NON-LINEAR DYNAMIC ANALYSES

The set of the far-fault ground motions of FEMA P695 [59] was used for the non-linear dynamic analyses of this study. This set comprises 22 record pairs, each with two horizontal components for a total of 44 records. The ground motions of the above set were recorded on stiff soil and at sites with distance larger than or equal to 10 km from fault rupture. The magnitudes of the earthquakes range from $M$ 6.5 to $M$ 7.6 with an average magnitude of $M$ 7.0. The records were scaled to DBE and MCE, using as intensity measure (IM) the 5% spectral acceleration at fundamental period $T_1$ of the frame models, $S_a(T_1)$.

## *5.1 Assessment of the seismic performance of the frames*

The results of the 44 non-linear dynamic analyses for the SC-MRF and sixteen SC-MRF-CBs were post-processed and the median maximum values of $\theta_{s,\max}$ of all the storeys and peak floor acceleration (PFA) from all the floors are shown in Table 3. The results in Table 3 indicate that the $\theta_{s,\max}$ of all SC-MRF-CBs is lower than that of the SC-MRF under the FOE, DBE and MCE seismic intensity levels. In particular, for the FOE intensity level, the relative reduction of the $\theta_{s,\max}$ of the SC-MRF-CBs compared to that of the SC-MRF ranges from 3.03% for the H35K167A5 to 23.65% for the H35K167A10. Under the DBE, the relevant minimum reduction of $\theta_{s,\max}$ is 1.42% and achieved for the H35K133A5 and the maximum is 24.13% and achieved for the H40K167A15. Under the MCE, the H35K133A5 achieves the minimum reduction of $\theta_{s,\max}$ equal to 0.95% and the H35K167A10 the maximum equal to 18.55%. Moreover, all the SC-MRF-CBs achieve $\theta_{s,\max}$ lower than the "life safety" and "collapse prevention" limits of EC8 [6] and ASCE/SEI 41-06 [60]. As it can be seen from Table 3, the SC-MRF-CBs achieve as much as a 24.05% overall $\theta_{s,max}$ reduction (minimum reduction between all seismic intensity levels for the H35K167A10). These results demonstrate that the new column base configuration is very effective in reducing $\theta_{s,\max}$, and that is done by only adjusting its base stiffness and strength characteristics.

Table 3. Median maximum values of $\theta_{s,\max}$ of all the storeys and PFA from all the floors of the SC-MRF and SC-MRF-CB design cases.

| Frame | Fundamental Period $T_1$ (s) | $\theta_{s,max}$ (%) | | | PFA (g) | | |
|---|---|---|---|---|---|---|---|
| | | FOE | DBE | MCE | FOE | DBE | MCE |
| SC-MRF | 0.94 | 0.655 | 1.814 | 2.623 | 0.499 | 1.043 | 1.487 |
| H40K133A5 | 0.95 | 0.547 | 1.667 | 2.416 | 0.506 | 0.980 | 1.481 |
| H40K133A15 | 0.95 | 0.530 | 1.529 | 2.336 | 0.534 | 0.932 | 1.385 |
| H40K167A15 | 0.93 | 0.519 | 1.376 | 2.170 | 0.521 | 0.932 | 1.362 |
| H40K167A5 | 0.93 | 0.621 | 1.671 | 2.494 | 0.520 | 1.036 | 1.462 |
| H40K133A10 | 0.95 | 0.530 | 1.510 | 2.319 | 0.526 | 0.918 | 1.356 |
| H40K167A10 | 0.93 | 0.531 | 1.433 | 2.264 | 0.542 | 0.954 | 1.316 |
| H40K133A24 | 0.95 | 0.530 | 1.448 | 2.294 | 0.519 | 0.919 | 1.508 |
| H35K133A5 | 0.95 | 0.576 | 1.788 | 2.598 | 0.509 | 0.911 | 1.428 |
| H35K133A15 | 0.95 | 0.542 | 1.655 | 2.353 | 0.506 | 0.918 | 1.341 |
| H35K167A15 | 0.93 | 0.501 | 1.384 | 2.147 | 0.489 | 0.903 | 1.416 |
| H35K167A5 | 0.93 | 0.635 | 1.745 | 2.538 | 0.556 | 0.966 | 1.418 |
| H35K133A10 | 0.95 | 0.546 | 1.683 | 2.379 | 0.495 | 0.910 | 1.392 |
| H35K167A10 | 0.93 | 0.500 | 1.396 | 2.136 | 0.494 | 0.899 | 1.400 |
| H35K200A10 | 0.91 | 0.506 | 1.534 | 2.140 | 0.504 | 0.887 | 1.367 |
| H35K133A20 | 0.95 | 0.522 | 1.542 | 2.299 | 0.515 | 0.914 | 1.364 |
| H30K133A10 | 0.95 | 0.543 | 1.667 | 2.299 | 0.470 | 0.864 | 1.364 |

The maximum values of PFA from all the floors of all the SC-MRF-CBs are lower than that of the SC-MRF under the DBE. Under the FOE and MCE, all the values of PFA of the SC-MRF-CBs are lower than that of the SC-MRF, with the exception of H35K167A5 and H40K133A24 for the FOE and MCE, respectively. The PFA reduction observed in the SC-MRF-CBs ranges from 5.81% to 23.65%, from 0.73% to 17.19% and from 0.42% to 11.46%, under the FOE, DBE and MCE, respectively. Thus, the new self-centering column bases can be very effective in reducing the PFA of an SC-MRF that will be equipped with these column bases.

These results show that the SC-MRF-CBs have in general better seismic performance than the SC-MRF in terms of the above two engineering demand parameters examined. Low values of $\theta_{\mathrm{s,max}}$ and PFA are associated with low non-structural and equipment damage. Thus, non-structural elements and equipment installed to SC-MRF-CBs may exhibit less damage. In addition, since $\theta_{\mathrm{s,max}}$ dictates the design of columns in the serviceability limit state, there is a potential of reducing the cross-sections of the members of the SC-MRF-CBs because they exhibit very low values of $\theta_{\mathrm{s,max}}$.

Figure 5 depicts the comparison of the height-wise distribution of $\theta_{\mathrm{s,max,}}$ of all the frames studied herein under the FOE, DBE and MCE. Under the FOE, the H40K167A15, H40K167A10, H40K133A24, H35K167A15, H35K167A10 and H35K200A10 have lower values of $\theta_{\mathrm{s,max,}}$ for all the storeys. The rest of the SC-MRF-CBs have lower values of $\theta_{\mathrm{s,max,}}$ for all the storeys, with the exception of the first storey. It is also observed that the SC-MRF-CBs have lower values of $\theta_{\mathrm{s,max,}}$ for all the storeys, with the exception of the first storey under the DBE level. The same trend is observed for all the frames at the MCE level, with the exception of H35K200A10, H35K167A15, H35A167A10 and H40K167A15, which have lower values of $\theta_{\mathrm{s,max}}$ for all the storeys. The reason for the increased first-storey $\theta_{s,max}$

demands of most of the SC-MRF-CBs is attributed to the gap openings of their self-centering column bases.

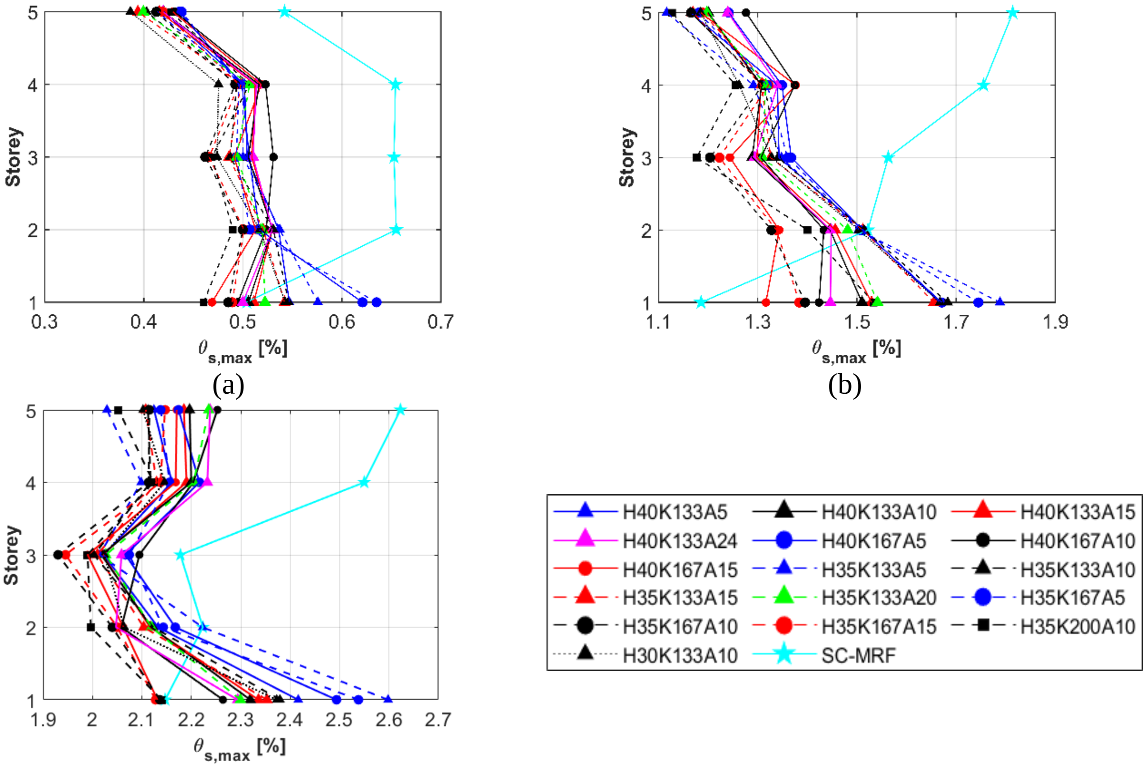

(a)
(b)
(c)

Figure 5 Comparison of the median height-wise distribution of the $\theta_{s,max}$ of the SC-MRF and SC-MRF-CB designs under the: (a) FOE; (b) DBE; and (c) MCE intensity levels.

Figure 6 shows the comparison of the height-wise distribution of PFA under the FOE, DBE and MCE. Under the FOE, apart from the H35K200A10, all the other SC-MRF-CBs have higher PFAs compared to that of the SC-MRF. In the second storey, all the SC-MRF-CBs have higher PFAs compared to that of the SAC-MRF. In the third storey, there is a shift in this trend; H30K133A10, H35K133A10, H40K133A24 and H35K133A15 have lower PFAs than that of the SC-MRF. In the fourth storey, only H35K133A5, H40K133A5, H35K167A5 and H40K167A5 have higher PFAs than that of the SC-MRF. Finally, in the fifth storey, apart from H40K167A5, all the other SC-MRF-CBs have lower PFAs compared to that of the SC-MRF. Under the DBE, the SC-MRF has PFAs lower than those of all the SC-MRF-CBs in both the first and second storey. However, in the third storey, apart from H35K167A4 and H40K176A5 which have higher PFAs, and H40K167A10 which has similar PFA, all the other SC-MRF-CBs have lower PFAs compared to that of the SC-MRF. Finally, in both the fourth and fifth storeys, all the SC-MRF-CBs have lower PFAs comparted to that of the SC-MRF. Under the MCE, apart from H35K133A15 that has lower PFA in its second storey, all the other SC-MRF-CBs have higher PFAs in all their three first storeys as compared to those of the SC-MRF. In the fourth storey, H40K167A15, H35K167A10 and H35K167A15 have lower PFAs as compared to the SC-MRF. Lastly, in the fifth storey, all the SC-MRF-CBs have lower PFAs compared to that of the SC-MRF.

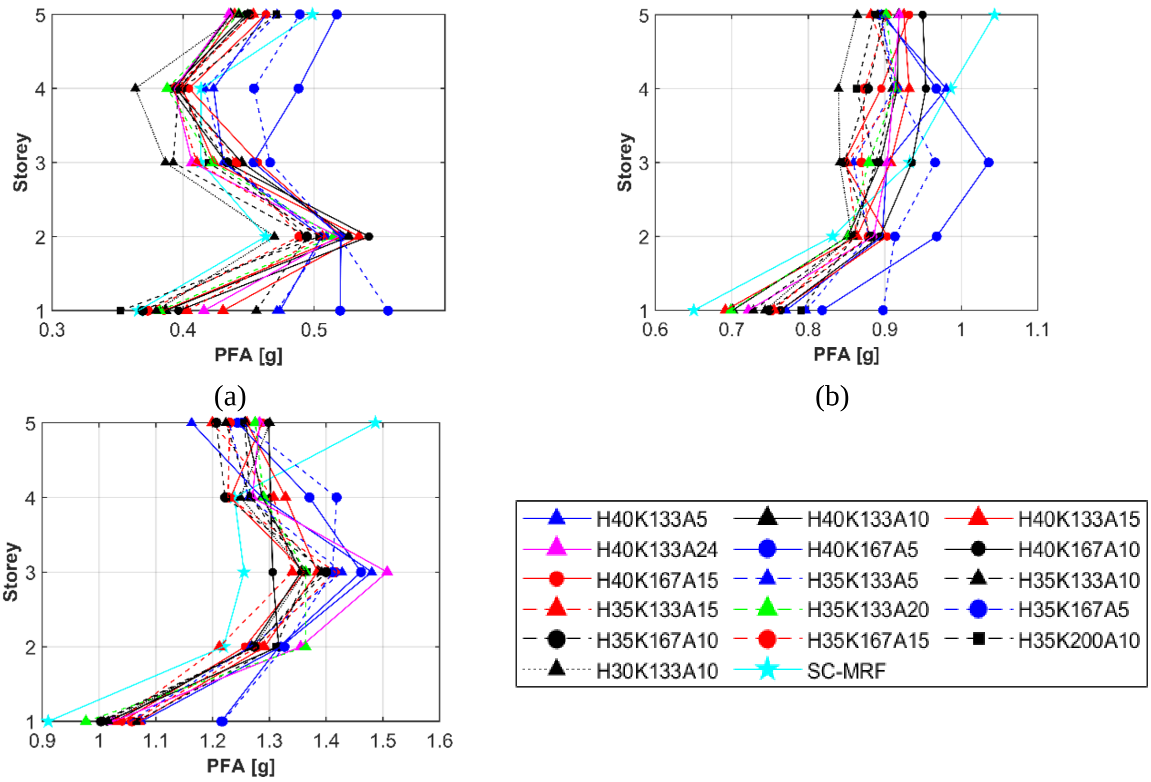

(a) (b)

(c)

Figure 6 Comparison of the median height-wise distribution of the PFA of the SC-MRF and SC-MRF-CBs under the: (a) FOE; (b) DBE; and (c) MCE intensity levels.

The PFA distribution of Figure 6 can be explained by recent studies in self-centering MRFs with connections similar to those of the SC-MRF-CBs. These suggest that the magnitudes of the PFAs and their distribution is influenced by the interactions between the beams and columns of these systems. These member interactions are due to the discontinuity of their connections and the asymmetry in member restraints due to the presence of the rocking in the column bases [61].

### 5.2 *Effect of base strength and stiffness on the seismic performance of the frames*

In this section, the effect of base strength and stiffness on the seismic performance of the frames examined herein is evaluated in terms of $\theta_{\mathrm{s,max}}$ and PFA. The parameters $\eta$, $\beta_{base}$ and $\alpha$, that are associated with the base strength and stiffness of the frames, were used for this evaluation.

In order to evaluate the effect of base strength of the frames to the response parameters $\theta_{\mathrm{s,max}}$ and PFA, the parameter $\eta$ is examined. Thus, the design cases H40K133A10, H35K133A10 and H30K133A10, with $\eta$ equals 0.40, 0.35 and 0.30, respectively, were compared. Figures 7(a) and 7(b) show $\theta_{\mathrm{s,max}}$ and PFA versus $\eta$, respectively, for the three seismic intensities examined. As indicated in Figure 7(a), when $\eta$ increases from 0.30 to 0.35, $\theta_{\mathrm{s,max}}$ also increases for all the seismic intensity levels. The increase observed is 0.65%, 0.93% and 3.36% under the FOE, DBE and MCE, respectively. A further increase of $\eta$ to 0.40 results in a reduction of $\theta_{\mathrm{s,max}}$ for all the seismic intensity levels. The reduction of $\theta_{\mathrm{s,max}}$ is 2.98%, 10.27% and 2.52% under the FOE, DBE and MCE, respectively. The same trend is observed for the PFA but only for the MCE intensity level. Under FOE and DBE, an increase of $\eta$ results in an increase of PFA. More specifically, when $\eta$ increases from 0.30 to 0.35, PFA values increase by 5.07% and 5.02%, under the FOE and DBE, respectively. A further increase of $\eta$ to 0.40 results in an increase of PFA equal to 6% and 0.94%, under the FOE and DBE, respectively.

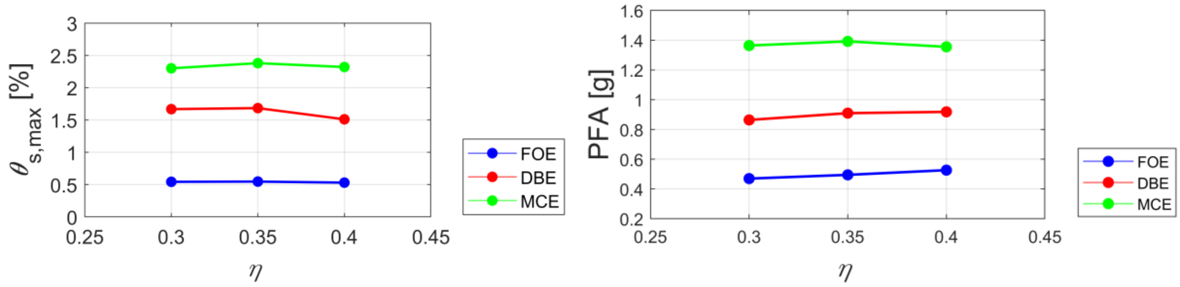

(a) (b)

Figure 7 Effect of $\eta$ to (a) $\theta_{\mathrm{s,max}}$; and (b) PFA.

The design cases examined herein were compared in terms of the parameters $\beta_{base}$ and $\alpha$ to evaluate the effect of base stiffness on their seismic response. For the frames with $\eta$=0.40, the following design cases were compared to evaluate the effect of $\beta_{base}$, i.e.: H40K133A5 ($\beta_{base}$=133%) and H40K167A5 ($\beta_{base}$=167%), which have a value of $\alpha$=5%; H40K133A10 ($\beta_{base}$=133%) and H40K167A10 ($\beta_{base}$=167%), with $\alpha$ = 10%; and H40K133A15 ($\beta_{base}$=133%) and H40K167A15, with $\alpha$=15%. For the frames with $\eta$=0.35, the following frames were compared: H35K133A5 ($\beta_{base}$=133%) and H35K167A5 ($\beta_{base}$=167%), with $\alpha$=5%; H35K133A10 ($\beta_{base}$=133%), H35K167A10 ($\beta_{base}$=167%) and H35K200A10 ($\beta_{base}$=200%), with $\alpha$=10%; and H35K133A15 ($\beta_{base}$=133%) and H35K167A15 $\beta_{base}$=167%), with $\alpha$=15%. Figure 8 shows the effect of $\beta_{base}$ to the seismic response, in terms of the $\theta_{\mathrm{s,max}}$ and PFA, of the aforementioned design cases.

For the frames with $\eta$=0.40 and $\alpha$=5%, the results in Table 3 show that an increase of $\beta_{base}$ from 133% to 167% results to higher values of $\theta_{s,max}$, for all the intensity levels. Thus, the increase of $\theta_{s,max}$ observed, due to the increase of $\beta_{base}$, is 11.91%, 0.25% and 3.11%, for the FOE, DBE and MCE seismic intensity levels, respectively. The same increase of $\beta_{base}$, leads to a reduction of $\theta_{s,max}$ for all the seismic intensity levels for the frames with $\eta$=0.40 and $\alpha$=10%. The reduction observed equals 2.09%, 10.01% and 7.09%, under the FOE, DBE and MCE, respectively. Finally, an increase of $\beta_{base}$ from 133% to 167% results to lower $\theta_{s,max}$ for the frames with $\eta$=0.40 and $\alpha$=15%, under the DBE and MCE. This trend is reversed under the FOE. In addition, the increase of $\beta_{base}$ from 133% to 167 results to higher values of PFA under the FOE and DBE, for the frames with $\eta$=0.40 and $\alpha$=5% and $\alpha$=10%. In contrary, the same increase of $\beta_{base}$ leads to a reduction of PFA under all the seismic intensity levels for the frames with $\eta$=0.40 and $\alpha$=15%.

For the frames with $\eta$=0.35 and $\alpha$=10% and $\alpha$=15%, results in Table 3 show that an increase of $\beta_{base}$ from 133% to 167% results to lower values of $\theta_{s,max}$, for all the seismic intensity levels. For the frames with $\alpha$=10%, the reduction of $\theta_{s,max}$, due to the increase of $\beta_{base}$, is 8.46%, 17.09% and 10.21%, under the FOE, DBE and MCE, respectively. For the frames with $\alpha$=10%, this reduction equals 7.56%, 16.40% and 8.76% under the FOE, DBE and MCE. In the frames with $\eta$=0.35 and $\alpha$=5%, an increase of $\beta_{base}$ from 133% to 167% results to 2.43% and 2.31% lower values of $\theta_{s,max}$, under the DBE and MCE, respectively. An opposite trend is observed under the FOE. For the frames with $\eta$=0.35 and $\alpha$=5%, results show that an increase of $\beta_{base}$ from 133% to 167% results to 8.46% and 5.63% higher values of PFA under the FOE and DBE, respectively. Under the MCE, the PFA of the frame with $\beta_{base}$=133% is 0.68% larger than that of with $\beta_{base}$=167%. For the frames with $\eta$=0.35 and $\alpha$=10%, results show that an increase of $\beta_{base}$ from 133% to 167% results to 0.08% and 1.14% lower values of PFA under the FOE and DBE, respectively. Under the MCE, the PFA of the frame with $\beta_{base}$=167% is 0.56% larger than that of with $\beta_{base}$=133%. A similar trend is observed for the frames with $\eta$=0.35 and $\alpha$=15%.

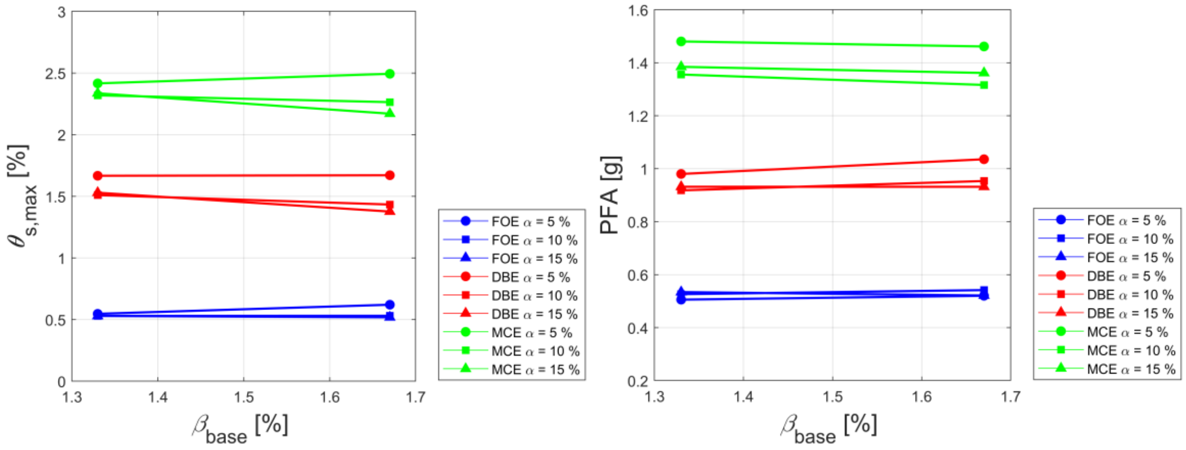

(a) (b)

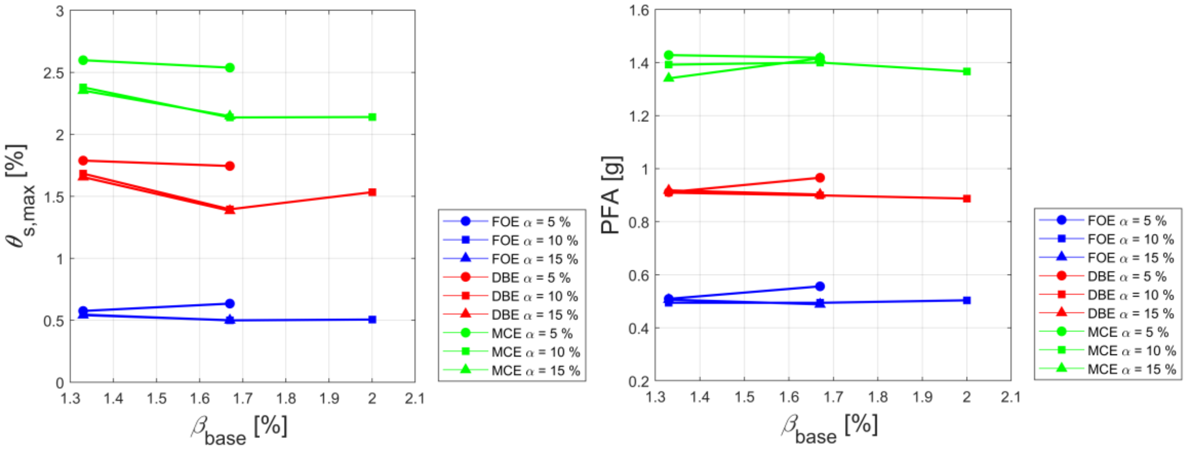

(c) (d)

Figure 8 Effect of $\beta_{base}$ to (a) $\theta_{s,\max}$ ($\eta$ = 0.40); (b) PFA ($\eta$ = 0.40); (c) $\theta_{s,\max}$ ($\eta$ = 0.35); and (d) (b) PFA ($\eta$ = 0.35).

For the design cases with $\eta$=0.40, the following frames were compared to evaluate the effect of $\alpha$ on $\theta_{s,max}$ and PFA: H40K133A5 ($\alpha$=5%), H40K133A10 ($\alpha$=10%), H40K133A15 ($\alpha$=15%) and H40K133A24 ($\alpha$=24.5%), with $\beta_{base}$=133%; and H40K167A5 ($\alpha$=5%), H40K167A10 ($\alpha$=10%) and H40K167A15 ($\alpha$=15%), with $\beta_{base}$=167%. This effect is shown in Figures 9(a)-(d) for these design cases. It is observed that the highest value of $\theta_{s,max}$ is achieved by H40K133A5 ($\alpha$=5%) for the frames with $\beta_{base}$=133%, under the FOE, DBE and MCE. The lowest values of $\theta_{s,max}$ are achieved for the frame H40K133A24 ($\alpha$=24.5%) for both the DBE and MCE. Frame H40K133A5 with $\alpha$=5% has the best PFA performance, achieving the lowest value of PFA under the FOE. In addition, the frame with $\alpha$=10% has the best PFA performance under the DBE and MCE. For the frames with $\beta_{base}$=167%, increasing the value of $\alpha$ from 5% to 10%, results in a reduction of $\theta_{s,max}$ for all the seismic intensity levels. This reduction equals 14.48%, 14.22% and 9.21%, under the FOE, DBE and MCE, respectively. A further increase of $\alpha$ from 10% to 15%, leads to a reduction of $\theta_{s,max}$, which equals 2.31%, 3.98% and 4.23%, under the FOE, DBE and MCE, respectively. Increasing the value of $\alpha$ from 5% to 10%, leads to a 3.95% increase, and 7.94% and 9.93% reduction of PFA under the FOE, DBE and MCE, respectively. Finally, a further increase of $\alpha$ from 10%

to 15%, leads to a 3.76% and 2.29% reduction and 3.32% increase of PFA, under the FOE, DBE and MCE, respectively.

For the design cases with $\eta$=0.35, the following frames were compared: H35K133A5 ($\alpha$=5%), H35K133A10 ($\alpha$=10%), H35K133A15 ($\alpha$=15%) and H35K133A20 ($\alpha$=20%), with $\beta_{base}$=133%; and H35K167A5 ($\alpha$=5%), H35K167A10 ($\alpha$=10%) and H35K167A15 ($\alpha$=15%), with $\beta_{base}$=167% (Figures 9(e)-(h)). For the frames with $\beta_{base}$=133%, the lowest values of $\theta_{s,max}$ is achieved for the frame with the higher value of $\alpha$, i.e., 20% (H35K133A20), for all the seismic intensity levels. The frame with $\alpha$=5% (H35K133A10) has the best PFA performance, achieving the lowest value of PFA under DBA and MCE. In addition, the frame $\alpha$=15% has the best PFA performance under the MCE. For the frames with $\beta_{base}$=167%, increasing the value of $\alpha$ from 5% to 10%, results in a reduction of $\theta_{s,max}$ for all the seismic intensity levels. This reduction equals 21.26%, 20.02% and 15.83%, under the FOE, DBE and MCE, respectively. A further increase of $\alpha$ from 10% to 15%, leads to a 0.23% increase, 0.83% reduction and 0.49% increase of $\theta_{s,max}$, under the FOE, DBE and MCE, respectively. Increasing the value of $\alpha$ from 5% to 10%, leads to a 11.14%, 6.89% and 1.30% reduction of PFA under the FOE, DBE and MCE, respectively. Finally, a further increase of $\alpha$ from 10% to 15%, results to a 1.14% reduction, and 0.38% and 1.14% increase of PFA, under the FOE, DBE and MCE, respectively.

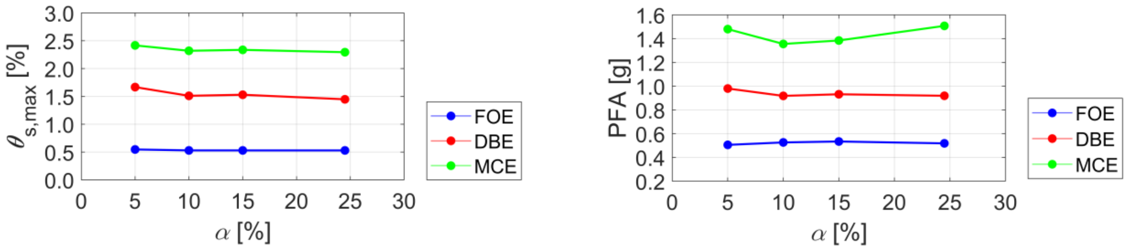

(a) (b)

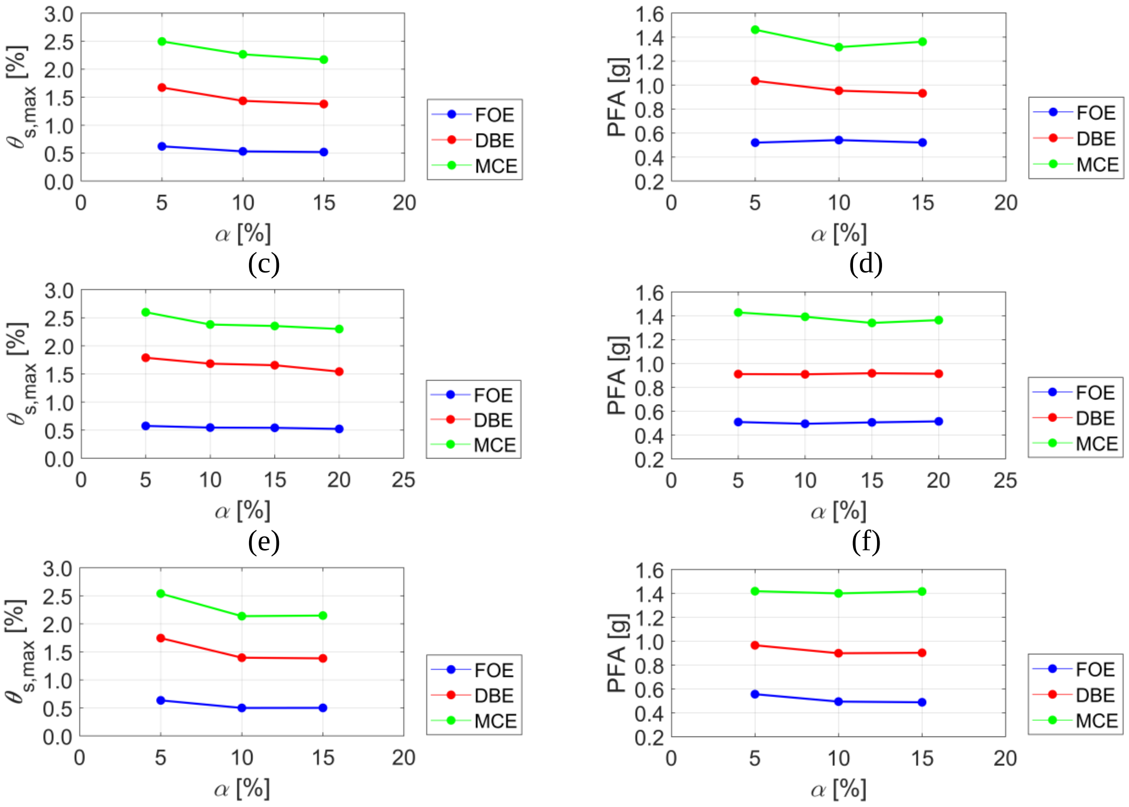

(c) (d)

(e) (f)

(g) (h)

Figure 9 Effect of $\alpha$ to (a) $\theta_{s,max}$ ($\eta$ = 0.40, $\beta_{base}$ = 133%); (b) PFA ($\eta$ = 0.40, $\beta_{base}$ = 133%); (c) $\theta_{s,max}$ ($\eta$ = 0.40, $\beta_{base}$ = 167%); (d) PFA ($\eta$ = 0.40, $\beta_{base}$ = 167%); (e) $\theta_{s,max}$ ($\eta$ = 0.35, $\beta_{base}$ = 133%); (f) PFA ($\eta$ = 0.35, $\beta_{base}$ = 133%); (g) $\theta_{s,max}$ ($\eta$ = 0.35, $\beta_{base}$ = 167%); and (h) PFA ($\eta$ = 0.35, $\beta_{base}$ = 167%).

### 5.3 *Residual drift performance of the frames*

Figure 10 shows the height-wise distribution of the median residual drifts ($\theta_{s,res}$) of the SC-MRF, H35K133A5 and H35K200A10 under the MCE, together with a maximum allowable limit for residual drifts. This limit was proposed by McCormick et al. [62] and utilised to characterise repairability in such buildings. The rationale for presenting only these two SC-MRF-CBs is that they are those that exhibit the lowest and highest $\theta_{s,res}$ values among the investigated frames. Residual drifts are recognised as an important index of the seismic performance and resilience of structures since they are directly linked to probability of demolition of a building [34,62]. It is observed that all the frames have values of $\theta_{s,res}$ lower than the proposed limit in [62] and that both H35K133A5 and H35K200A10 have lower $\theta_{s,res}$ values for all their storeys than those of the SC-MRF. These values are almost negligible.

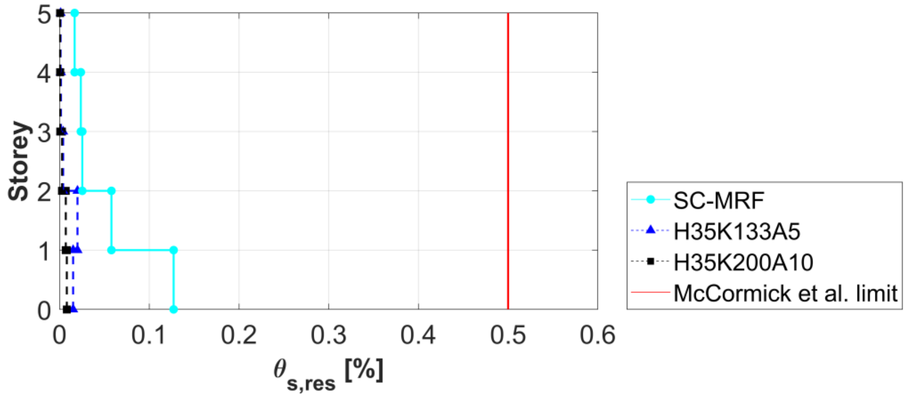

Figure 10 Height-wise distribution of median residual drifts of the SC-MRF, H35K133A5 and H35K200A10 under the MCE, plotted against the maximum allowable limit for residual interstorey drifts proposed by McCormick et al. [62].

Figure 11 shows the stress-strain hysteresis loops in the flanges of the first-storey columns (Figure 3(a)) of the H35K133A5 and H35K200A10 under the 1992 Landers earthquake scaled to the MCE. It is observed, that the two SC-MRF-CBs do not exhibit any plastic deformation in their first-storey columns since the developed maximum stress at the extreme fibers of their flanges is well below the yield stress limit of 355 MPa. Thus, damage is avoided at their self-centering column bases. This shows that the values of $\theta_{s,res}$ observed in SC-MRF-CBs (Figure 10) mainly result from permanent deformations that occur at PT beam-column connections. Similar results are observed for the rest of the SC-MRF-CBs and ground motions but are not shown herein due to lack of space.

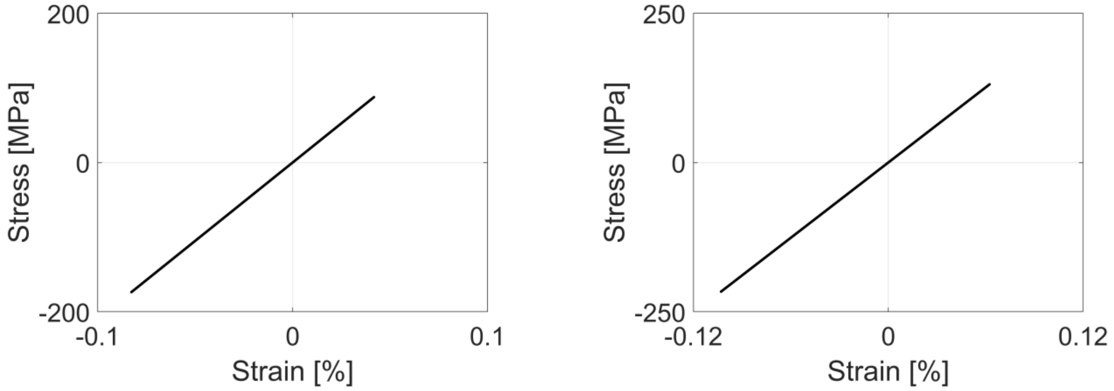

(a) (b)

Figure 11 Stress strain hysteresis loops of a flange of a first storey column of: (a) H35K133A5; and (b) H35K200A10 under the 1992 Landers earthquake scaled to MCE.

## 6 COLLAPSE ASSESSMENT

The collapse resistance of the frames is determined by the use of IDA [63]. $S_a(T_1)$ is the IM used herein and $\theta_{s,max}$ was the response parameter monitored. The set of ground motions used for the non-linear dynamic analyses in Section 5 were used also for the IDAs. For each design case and ground motion, the collapse $S_a(T_1)$ value at which $\theta_{s,max}$ increases without bound was obtained. To determine the limit of collapse, the criterion adopted by Seo et al. [64] was used. Thus, the incremental slopes were calculated by drawing straight lines between the consecutive data points in the IDA curve. The lowest $S_a(T_1)$ value corresponding to the $i^{th}$ data point with the slope between the $i^{th}$ and $i+1^{th}$ points being less than 10% of the initial slope on the IDA curve was defined as the collapse $S_a(T_1)$. The initial slope was determined from the straight line from the origin of axis to the first data point of the IDA curve. A collapse fragility curve was generated by fitting a lognormal cumulative distribution function to the collapse $S_a(T_1)$ values determined for each frame. The median value, $S_{CT}$, and the lognormal standard deviation, $\beta$, of collapse $S_a(T_1)$ values define this distribution. The value of $S_{CT}$ was amplified to take into account the effect of the distinct spectral shape of rare ground motions, characterised by the parameter $\varepsilon$ [65]. In this work, the simplified methodology proposed by FEMA P695 [59] is adopted, where the influence of the spectral shape is taken into account by the use of a spectral shape factor (*SSF*). Thus, the values of $S_{CT}$ of all the frames of this study were multiplied by *SSF* to estimate their true collapse capacity.

The parameter $\beta$ affects the shape of the fragility curve and is a measure of the level of uncertainty in the analysis results. The system-level and the record-to-record uncertainty were used for the construction of the fragility curves. The FEMA P695 [59] regulations were used for the calculation of the total uncertainty, where additional system-level uncertainty were added from three categories [43]. The total uncertainty of the system, $\beta_{Total}$, is given by:

$$\beta_{Total} = \sqrt{\beta_{RTR}^2 + \beta_{DR}^2 + \beta_{TD}^2 + \beta_{MDL}^2} \tag{13}$$

where $\beta_{RTR}$ is the record-to-record uncertainty, $\beta_{DR}$, $\beta_{TD}$ and $\beta_{MDL}$ are the additional uncertainty because of the robustness of the design requirements, the accuracy of the test data and the accuracy of the numerical model, respectively. The values of $\beta_{RTR}$ were taken from the results of the IDA, while values of the rest uncertainties were based on P695 recommendations [59]. Thus, the uncertainties $\beta_{DR}$, $\beta_{TD}$ and $\beta_{MDL}$ can be subjectively classified as 'superior', 'good', 'fair', or 'poor' [59]. The uncertainty due to the robustness of the design requirements, accuracy of the test data and numerical model were assigned each rating of 'superior', 'good', 'fair' and 'poor' together to construct four different collapse fragility curves. The values of uncertainty for 'superior', 'good', 'fair' and 'poor' uncertainty rating were 0.1, 0.2, 0.35 and 0.5, respectively. Figure 12 shows the IDA curves of the H35K200A10 together with the collapse fragility curves, for different uncertainty ratings as per the aforementioned procedure.

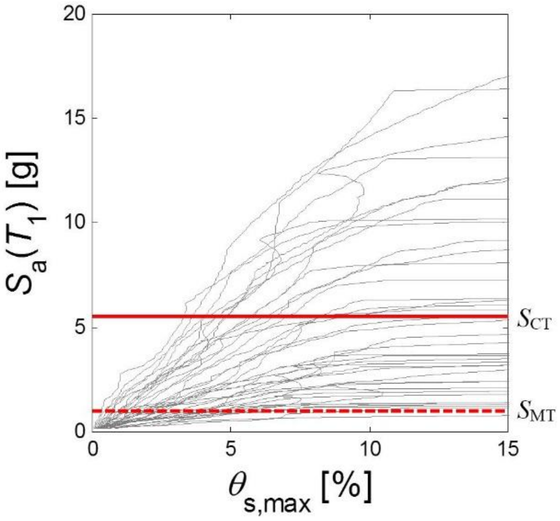

(a)

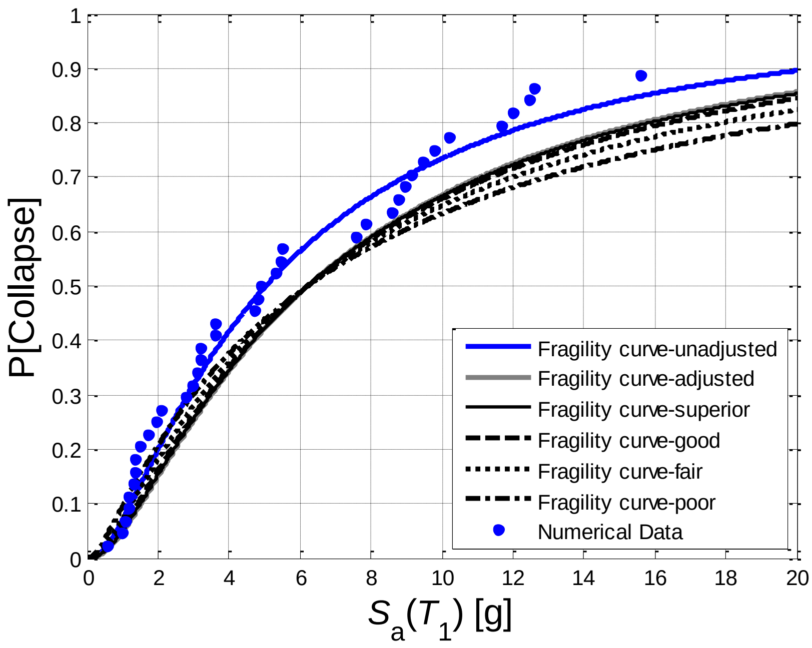

(b)

Figure 12 (a) IDA curves; and (b) corresponding collapse fragility curves of the H35K200A10.

Finally, the constructed collapse fragility curves were used for the evaluation of the collapse risk of the frames through the adjusted collapse margin ratio (*ACMR*), defined as:

$$ACMR = \frac{S_{CT}}{S_{MT}} \cdot SSF \tag{14}$$

where $S_{\mathrm{CT}}$, is the median collapse intensity of the frames, $S_{\mathrm{MT}}$ is intensity demand to the MCE-level intensity.

## 7 EFFECT OF BASE STRENGTH AND STIFFNESS ON THE COLLAPSE RISK OF THE FRAMES

Table 4 shows the collapse capacity results of all the investigated frames. The SC-MRF-CBs have larger value of collapse capacity and *ACMR*, compared to the SC-MRF. The maximum increase in collapse capacity and *ACMR* is achieved by the H35K200A10 compared to SC-MRF, whereas the minimum increase of these parameters is achieved by the H35K133A5. Collapse capacity and *ACMR* of the SC-MRF-CBs design cases are 25.08-33.23% and 23.02-27.95% higher, respectively, than that of the SC-MRF. Thus, there is a significant improvement of the collapse capacity and *ACMR*, by adopting the self-centering column bases and appropriately tuning their base stiffness and strength characteristics.

Figure 13 shows the collapse fragility curves of the SC-MRF, H35K133A5 and H35K200A10 for different uncertainty ratings. These two SC-MRF-CBs were selected because they achieve the lower and higher increase of *ACMR*, compared to the SC-MRF. It is observed that the H35K133A5 and H35K200A10 are exhibiting, in general, the lowest probabilities of collapse. This trend is inverted for low values of $S_a(T_1)$, for superior, good and fair uncertainty ratings, and for poor uncertainty ratings the probabilities of collapse are similar for all the frames.

Table 4. Collapse capacity results.

| Frame | $S_{MT}$ (g) | $S_{CT}$ (g) | *CMR* | *SSF* | *ACMR* |
|---|---|---|---|---|---|
| SC-MRF | 0.90 | 3.70 | 4.10 | 1.23 | 5.06 |
| H40K133A5 | 0.93 | 5.04 | 5.44 | 1.23 | 6.72 |
| H40K133A15 | 0.93 | 5.17 | 5.57 | 1.23 | 6.88 |
| H40K167A15 | 0.95 | 5.39 | 5.67 | 1.23 | 6.97 |
| H40K167A5 | 0.95 | 5.28 | 5.56 | 1.23 | 6.83 |
| H40K133A10 | 0.93 | 5.19 | 5.60 | 1.23 | 6.92 |
| H40K167A10 | 0.95 | 5.38 | 5.66 | 1.23 | 6.95 |
| H40K133A24 | 0.92 | 5.04 | 5.45 | 1.24 | 6.74 |
| H35K133A5 | 0.93 | 4.94 | 5.32 | 1.23 | 6.57 |
| H35K133A15 | 0.93 | 5.18 | 5.59 | 1.23 | 6.87 |
| H35K167A15 | 0.95 | 5.32 | 5.60 | 1.23 | 6.89 |
| H35K167A5 | 0.95 | 5.27 | 5.54 | 1.23 | 6.80 |
| H35K133A10 | 0.93 | 5.19 | 5.60 | 1.23 | 6.91 |
| H35K167A10 | 0.95 | 5.35 | 5.64 | 1.23 | 6.92 |
| H35K200A10 | 0.97 | 5.54 | 5.74 | 1.22 | 7.02 |
| H35K133A20 | 0.93 | 5.04 | 5.43 | 1.23 | 6.70 |
| H30K133A10 | 0.93 | 5.11 | 5.51 | 1.23 | 6.81 |

To evaluate the effect of base strength on the collapse risk of the frames, the base strength factor $\eta$ was utilised. To this end, the design cases H40K133A10, H35K133A10 and H30K133A10, with $\eta$ equals 0.40, 0.35 and 0.30, respectively, were compared. The H40K133A10 has the largest value of *ACMR* among the frames compared, indicating that the frame with the largest value of $\eta$ has the lowest collapse risk. When the value of $\eta$ is increased from 0.30 to 0.35, the *ACMR* is increased by 1.5%. In addition, the value of *ACMR* for the H40K133A10 with $\eta$ = 0.40 is 1.61% higher than that of the H30K133A10 with $\eta$ = 0.30. Thus, the collapse risk of the frames is reduced for higher values of $\eta$.

The frames examined here were compared in terms of their base factors $\beta_{base}$ and $\alpha$ to assess the effect of base stiffness on their collapse risk. For the frames with $\eta$=0.40, the following frames were compared to evaluate the effect of $\beta_{base}$, i.e.: H40K133A5 ($\beta_{base}$=133%) and H40K167A5 ($\beta_{base}$=167%), which have a value of $\alpha$=5%; H40K133A10 ($\beta_{base}$=133%) and H40K167A10 ($\beta_{base}$=167%), with $\alpha$=10%; and H40K133A15 ($\beta_{base}$=133%) and H40K167A15, with $\alpha$=15%. For the frames with $\eta$=0.35, the following frames were compared: H35K133A5 ($\beta_{base}$=133%) and H35K167A5 ($\beta_{base}$=167%), with $\alpha$=5%; H35K133A10 ($\beta_{base}$=133%), H35K167A10 ($\beta_{base}$=167%) and H35K200A10 ($\beta_{base}$=200%), with $\alpha$=10%; and H35K133A15 ($\beta_{base}$=133%) and H35K167A15 ($\beta_{base}$=167%), with $\alpha$=15%.

The results in Table 4 indicate that an increase of $\beta_{base}$ from 133% to 167% results to higher values of *ACMR* for the frames with $\eta$=0.40. Thus, the increase of *ACMR* observed, due to the increase of $\beta_{base}$, is 1.63%, 0.46% and 1.21% for the design cases with $\alpha$ equals 5%, 10% and 15%, respectively. Similar results are obtained for the frames with $\eta$=0.35. The values of *ACMR* of the frames with $\beta_{base}$ equal to 167% are 3.40%, 0.12% and 0.29% higher than those of the frames with $\beta_{base}$ equal to 133%, when $\alpha$ equals 5%, 10% and 15%, respectively. In addition, the frame H35K200A10 ($\beta_{base}$=200%) has 1.46% and 1.58% higher values of *ACMR* than those of the H35K167A10 ($\beta_{base}$=167%) and H35K133A10 ($\beta_{base}$=133%), respectively. Thus, it can be concluded that the collapse resistance of the frames is increased for frames with higher values of $\beta_{base}$, representing the initial base stiffness.

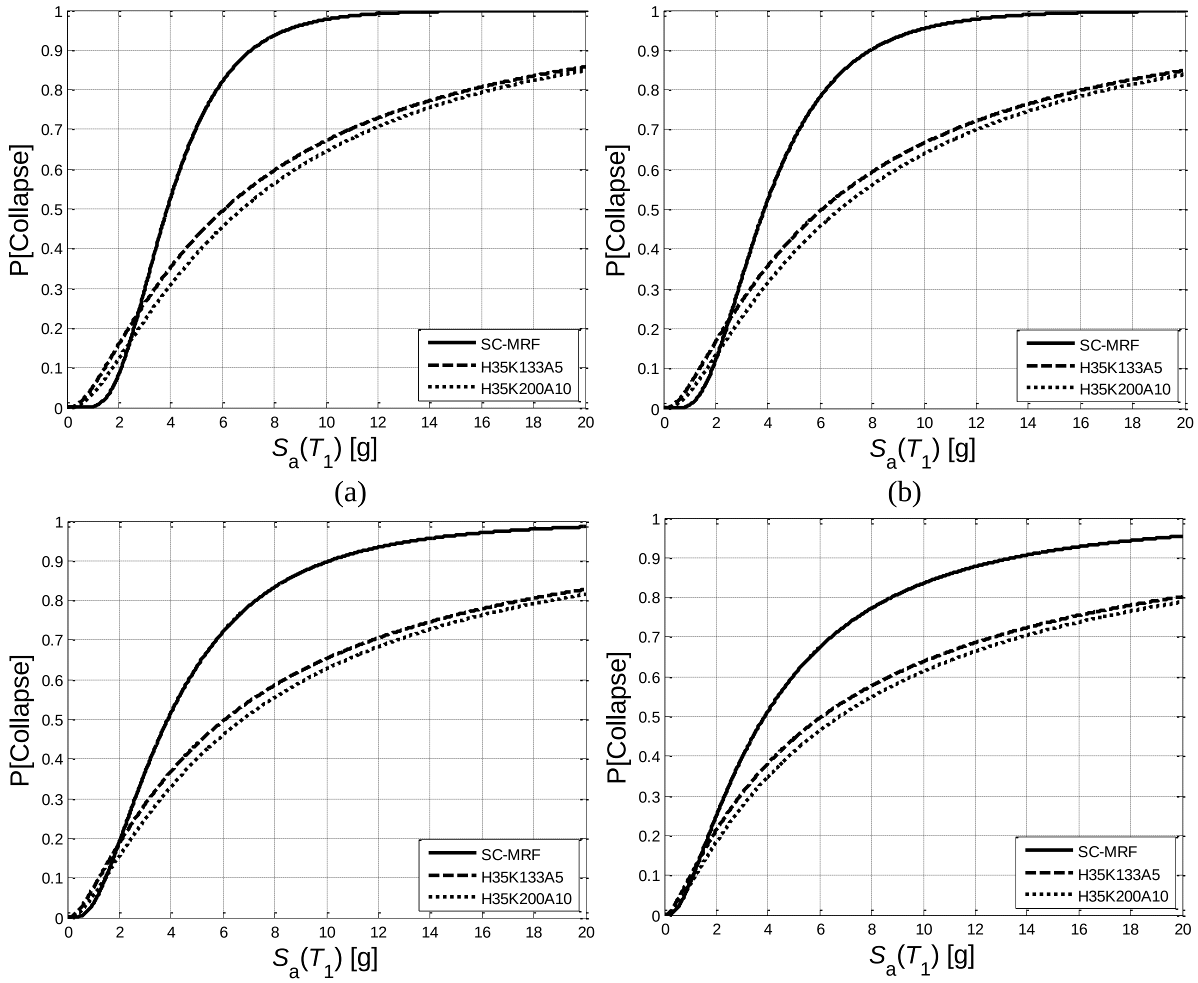

(a) (b)

(c) (d)

Figure 13 Collapse fragility curves of SC-MRF, H35K133A5 and H35K200A10 for: (a) superior; (b) good; (c) fair; and (d) poor uncertainty rating.

For the design cases with $\eta$=0.40, the following frames were compared to evaluate the effect of $\alpha$: H40K133A5 ($\alpha$=5%), H40K133A10 ($\alpha$=10%), H40K133A15 ($\alpha$=15%) and H40K133A24 ($\alpha$=24.5%), with $\beta_{base}$=133%; and H40K167A5 ($\alpha$=5%), H40K167A10 ($\alpha$=10%) and H40K167A15 ($\alpha$=15%), with $\beta_{base}$=167%. The results indicate that the higher value of *ACMR* is achieved by H40K133A10 ($\alpha$=10%), for the frames with $\beta_{base}$=133%. Thus, collapse resistance of the frames is increased by 2.89% when $\alpha$ increases from 5% to 10%, and is then reduced for further increase of $\alpha$. For the frames with $\beta_{base}$=167% a different trend is observed, with *ACMR* having higher values when $\alpha$ increases. Thus, the frame H40K167A15 ($\alpha$=15%) has 0.22% and 1.96% higher values of *ACMR* than those of H40K167A10 ($\alpha$=10%) and H40K167A5 ($\alpha$=5%), respectively.

For the design cases with $\eta$=0.35 the following frames were compared: H35K133A5 ($\alpha$=5%), H35K133A10 ($\alpha$=10%), H35K133A15 ($\alpha$=15%), and H35K133A20 ($\alpha$=20%), with $\beta_{base}$=133%; and H35K167A5 ($\alpha$=5%), H35K167A10 ($\alpha$=10%) and H35K167A15 ($\alpha$=15%), with $\beta_{base}$=167%. The results of the frames with $\beta_{base}$=133% demonstrate that the *ACMR* is increased when $\alpha$ is increased from 5% to 15% and is then reduced for further increase of $\alpha$. A similar trend is observed for the frames with $\beta_{base}$=167%.

# 8 CONCLUSIONS

The potential of the SC-MRF-CBs to improve the seismic performance and reduce the collapse risk of earthquake-resilient steel buildings with SC-MRFs was examined. The effect of strength and stiffness characteristics of the novel self-centering column base to improve the seismic performance and collapse capacity of the SC-MRF-CBs was also investigated. The parameters through which these effects were taken into consideration were three normalised factors that represent the initial stiffness, post-yield stiffness and strength of the self-centering column bases. These structural properties of the self-centering column bases can be independently adjusted by utilising the analytical expressions that are presented in this research, thereby changing also the initial stiffness, post-yield stiffness and strength of the whole SC-MRF-CBs. A design procedure for the self-centering column bases, which is enhanced compared to that in [29], is also proposed to that purpose. The evaluation of the seismic performance and collapse risk of the SC-MRF-CBs was based on a prototype steel building designed to incorporate different seismic-resistant frames, i.e., one SC-MRF and sixteen SC-MRF-CBs' designs with different base stiffness and strength characteristics. A set of 44 ground motions that were scaled to three seismic intensity levels was utilised to perform non-linear dynamic analyses and evaluate the seismic performance of the frames. Moreover, IDA was used with the same set of ground motions to evaluate the collapse capacity of the frames. Finally, fragility curves and the *ACMR* of the frames were derived to compare their seismic risk.

On the basis of the findings of this paper, the following conclusions can be drawn:

1. The SC-MRF-CBs have in general better seismic performance than the SC-MRF in terms of $\theta_{\mathrm{s,max}}$ and PFA. The results demonstrate that the self-centering column base is very effective in reducing $\theta_{\mathrm{s,max}}$ and PFA, by only tuning its base stiffness and strength characteristics. Thus, non-structural elements and equipment installed to SC-MRF-CBs will potentially exhibit less damage. A potential of reducing the cross-sections of the members of the SC-MRF-CBs can be also concluded. That is because the SC-MRF-CBs exhibit $\theta_{\mathrm{s,max}}$ values lower than the relevant limits of EC8 under the FOE, DBE and MCE. This reduction reaches an appreciable 24.05%.
2. The H35K133A5 and H35K200A10 (i.e., the two frames that exhibit the lowest and highest values of $\theta_{s,res}$ among the investigated SC-MRF-CBs) have lower values of $\theta_{\mathrm{s,res}}$ in all their storeys, compared to those of the SC-MRF. These values are almost negligible and are solely due to permanent deformations in the PT beam-column connections since the self-centering column bases behave elastically up to their targeted rotations.
3. The SC-MRF-CBs have superior collapse capacity compared to the SC-MRF. The collapse capacity and *ACMR* of the SC-MRF-CBs are increased by up to 33.23% and 27.95%, respectively, compared to the SC-MRF.
4. The collapse risk of the SC-MRF-CBs is reduced for higher values of $\eta$. The H40K133A10 with $\eta$=0.40 has the largest value of *ACMR* and thus the lowest collapse risk compared to the frames with $\eta$ equal to 0.35 and 0.30.
5. It is concluded that collapse capacity of the frames is increased for frames with higher values of $\beta_{base}$. The SC-MRF-CBs with $\beta_{base}$=167% have superior collapse resistance

than the ones with $\beta_{base}$=133%, when $\eta$=0.40. The maximum increase of *ACMR* observed, due to the increase of $\beta_{base}$, is 1.63% for the design cases with $\alpha$=5%. Similar results are obtained for the frames with $\eta$=0.35. The values of *ACMR* of the frames with $\beta_{base}$=167% are 3.40%, 0.12% and 0.29% higher than those of the frames with $\beta_{base}$=133%, when $\alpha$ equals 5%, 10% and 15%, respectively. In addition, the frame H35K200A10 ($\beta_{base}$=200%) has 1.46% and 1.58% higher values of *ACMR* than those of the H35K167A10 ($\beta_{base}$=167%) and H35K133A10 ($\beta_{base}$=133%), respectively.

6. The results for the SC-MRF-CBs with $\eta$=0.40 indicate that the higher value of *ACMR* is achieved by the frame with $\alpha$=10%, for the frames with $\beta_{base}$=133%. Thus, the collapse capacity of the frames increases by 2.89% when $\alpha$ increases from 5% to 10% and is then reduced for further increase of $\alpha$. For the frames with $\beta_{base}$=167%, a different trend is observed, with *ACMR* having higher values when $\alpha$ is increased up to 15%.
7. For the SC-MRF-CBs with $\eta$=0.35 and $\beta_{base}$=133%, it is observed that the *ACMR* is increased when $\alpha$ is increased from 5% to 15% and is then reduced for further increase of $\alpha$. A similar trend is observed for the frames with $\beta_{base}$=167%. Thus, an increase of $\alpha$ up to a certain value leads to an increase of the collapse capacity of the frames. It is also concluded that $\alpha$ is more effective in increasing the collapse capacity of the frames compared to $\beta_{base}$, because a similar increase of the collapse capacity is achieved by increasing both parameters, but for a larger increase of $\beta_{base}$.
8. It is concluded that the best seismic performance and highest collapse capacity among the SC-MRF-CBs examined is achieved for a combination of the strength factor, $\eta$, equal to 0.35; initial stiffness factor, $\beta_{base}$, equal to 200%; and post-yield stiffness ratio, $\alpha$, equal to 10%.

## REFERENCES

[1] H. Inamasu, D.G. Lignos, A.M. Kanvinde, Effect of column base flexibility on the hysteretic response of wide flange steel columns, 3rd Huixian Int. Forum Earthq. Eng. Young Res. August 11-12. (2017) Paper No. 260. https://infoscience.epfl.ch/record/230104/files/260_Inamasu_Hiroyuki_fullpaper.pdf.

[2] F. Zareian, A. Kanvinde, Effect of column-base flexibility on the seismic response and safety of steel moment-resisting frames, Earthq. Spectra. 29 (2013) 1537–1559. doi:10.1193/030512EQS062M.

[3] J. Ruiz-García, A. Kanvinde, Effect of column base flexibility on residual drift demands of low-rise steel moment-resisting frames, in: 2013 World Congr. Adv. Struct. Eng. Eng. Mech. (ASEM13), Sept. 8-12, Jeju, Korea, 2013: pp. 627–639.

[4] P.A. Torres-Rodas, F. Flores, F. Zareian, Seismic response of steel moment frame considering gravity system and column base flexibility, in: Proc. 11th US Natl. Conf. Earthq. Eng., June 25-29, Los Angeles, USA, 2018. https://www.researchgate.net/profile/Pablo_Torres-Rodas/publication/327663389_Seismic_Response_of_Steel_Moment_Frames_considering_gravity_system_and_column_base_flexibility/links/5b9c618292851ca9ed0aa655/Seismic-Response-of-Steel-Moment-Frames-considering.

[5] A. Aviram, B. Stojadinovic, A. Der Kiureghian, Performance and reliability of exposed column base plate connections for steel moment-resisting frames, Berkeley, CA, USA, 2010.

[6] BS EN 1998-1, Eurocode 8: Design of structures for earthquake resistance - Part 1: General rules, seismic actions and rules for buildings., 2013.

[7] P.T. Rodas, F. Zareian, A. Kanvinde, Hysteretic Model for Exposed Column–Base Connections, J. Struct. Eng. (2016) 04016137. doi:10.1061/(ASCE)ST.1943-541X.0001602.

[8] D.G. Lignos, H. Krawinkler, A database in support of modeling of component deterioration for collapse prediction of steel frame structures, in: John W. Wallace (Ed.), Struct. Eng. Res. Front. May 16-19, Long Beach, California, United States, 2007: pp. 1–12. doi:doi: 10.1061/40944(249)31.

[9] H.-J. Kim, C. Christopoulos, Seismic design procedure and seismic response of post-tensioned self-centering steel frames, Earhtquake Eng. Struct. Dyn. 38 (2009) 355–376. doi:10.1002/eqe.859.

[10] A.S. Tzimas, A.I. Dimopoulos, T.L. Karavasilis, EC8-based seismic design and assessment of self-centering steel frames with viscous dampers, J. Constr. Steel Res. 105 (2015) 60–73.

[11] J.M. Ricles, R. Sause, M.E.M. Garlock, C. Zhao, Posttensioned seismic-resistant connections for steel frames, J. Struct. Eng. 127 (2001) 113–121.

[12] K.-C. Tsai, C.-C. Chou, C.-L. Lin, P.-C. Chen, S.-J. Jhang, Seismic self-centering steel beam-to-column moment connections using bolted friction devices, Earthq. Eng. Struct. Dyn. 37 (2008) 627–645. doi:10.1002/eqe.779.

[13] G. Vasdravellis, T.L. Karavasilis, B. Uy, Large-scale experimental validation of steel post-tensioned connections with web hourglass pins, J. Struct. Eng. 139 (2013) 1033–42. doi:10.1061/(ASCE)ST.1943-541X.0000696.

[14] G. Vasdravellis, T.L. Karavasilis, B. Uy, Design rules, experimental evaluation, and fracture models for high-strength and stainless-steel hourglass shape energy dissipation devices, J. Struct. Eng. 140 (2014) 04014087. doi:10.1061/(ASCE)ST.1943-541X.0001014.

[15] P. Rojas, J.M. Ricles, R. Sause, Seismic Performance of Post-tensioned Steel Moment

Resisting Frames with Friction Devices, J. Struct. Eng. 131 (2005) 529–540. doi:10.1061/(ASCE)0733-9445(2005)131:4(529).

[16] C.-C. Chou, Y.-C. Wang, J.-H. Chen, Seismic design and behavior of post-tensioned steel connections including effects of a composite slab, Eng. Struct. 30 (2008) 3014–3023. doi:10.1016/j.engstruct.2008.04.013.

[17] M.A. Chowdhury, A. Rahmzadeh, M.S. Alam, Improving the seismic performance of post-tensioned self-centering connections using SMA angles or end plates with SMA bolts, Smart Mater. Struct. 28 (2019) 075044.

[18] M.A. Chowdhury, A. Rahmzadeh, S. Moradi, M.S. Alam, Feasibility of using reduced length superelastic shape memory alloy strands in post-tensioned steel beam–column connections, J. Intell. Mater. Syst. Struct. 30 (2018) 283–307. doi:10.1177/1045389X18806393.

[19] B. Uy, Innovative connections for the demountability and rehabilitation of steel, space and composite structures, in: 12th Int. Conf. Steel, Sp. Compos. Struct. 28-30 May, Prague, Czech Republic, 2014: pp. 99–109.

[20] J. Liu, Design for Deconstruction with Demountable Composite Beams and Floor Systems, Eng. J. 53 (2016) 107–16.

[21] S. Pampanin, C. Christopoulos, M.J.N. Priestley, Performance-based seismic response of frame structures including residual deformations. Part II: Multi-degree of freedom systems., J. Earthq. Eng. 7 (2003) 119–147.

[22] C. Christopoulos, A. Filiatrault, B. Folz, Seismic response of self-centring hysteretic SDOF systems, Earthq. Eng. Struct. Dyn. 31 (2002) 1131–1150. doi:10.1002/eqe.152.

[23] C. Christopoulos, Frequency Response of Flag-Shaped Single Degree-of-Freedom Hysteretic Systems, J. Eng. Mech. 130 (2004) 894–903. doi:10.1061/(ASCE)0733-9399(2004)130:8(894).

[24] C. Christopoulos, S. Pampanin, M.J.N. Priestley, Performance-based seismic response of frame structures including residual deformations. Part 1: Single-degree of freedom systems., J. Earthq. Eng. 7 (2003) 97–118.

[25] T.L. Karavasilis, C.-Y. Seo, Seismic structural and non-structural performance evaluation of highly damped self-centering and conventional systems, Eng. Struct. 33 (2011) 2248–2258. doi:10.1016/j.engstruct.2011.04.001.

[26] G.P. Cimellaro, Simultaneous stiffness–damping optimization of structures with respect to acceleration, displacement and base shear, Eng. Struct. 29 (2007) 2853–2870. doi:10.1016/j.engstruct.2007.01.001.

[27] C.-C. Chou, J.-H. Chen, Analytical model validation and influence of column bases for seismic responses of steel post-tensioned self-centering MRF systems, Eng. Struct. 33 (2011) 2628–2643. doi:10.1016/j.engstruct.2011.05.011.

[28] BS EN 1998-3, Eurocode 8 : Design of structures for earthquake resistance — Part 3: Assessment and retrofitting of buildings., 2005.

[29] V.C. Kamperidis, T.L. Karavasilis, G. Vasdravellis, Self-centering steel column base with metallic energy dissipation devices, J. Constr. Steel Res. 149 (2018) 14–30. doi:10.1016/j.jcsr.2018.06.027.

[30] H. Chi, J. Liu, Seismic behavior of post-tensioned column base for steel self-centering moment resisting frame, J. Constr. Steel Res. 78 (2012) 117–130. doi:10.1016/j.jcsr.2012.07.005.

[31] X.-T. Wang, C.-D. Xie, L.-H. Lin, J. Li, Seismic behavior of self-centering concrete-filled square steel tubular (CFST) Column Base, J. Constr. Steel Res. 156 (2019) 75–85. doi:https://doi.org/10.1016/j.jcsr.2019.01.025.

[32] M. Latour, G. Rizzano, A. Santiago, L. Simões da Silva, Experimental response of a low-yielding, self-centering, rocking column base joint with friction dampers, Soil

Dyn. Earthq. Eng. 116 (2019) 580–592. doi:https://doi.org/10.1016/j.soildyn.2018.10.011.

[33] B. Wang, S. Zhu, C.-X. Qiu, H. Jin, High-performance self-centering steel columns with shape memory alloy bolts: Design procedure and experimental evaluation, Eng. Struct. 182 (2019) 446–458. doi:https://doi.org/10.1016/j.engstruct.2018.12.077.

[34] FEMA, FEMA P-58-1 Seismic performance assessment of buildings - Volume 1 - Methodology (2nd Edition), Washington, DC, USA, 2018. https://www.fema.gov/media-library/assets/documents/90380.

[35] A.S. Tzimas, G.S. Kamaris, T.L. Karavasilis, C. Galasso, Collapse risk and residual drift performance of steel buildings using post-tensioned MRFs and viscous dampers in near-fault regions, Bull. Earthq. Eng. 14 (2016) 1643–1662. doi:10.1007/s10518-016-9898-3.

[36] A.I. Dimopoulos, T.L. Karavasilis, G. Vasdravellis, B. Uy, Seismic design, modelling and assessment of self-centering steel frames using post-tensioned connections with web hourglass shape pins, Bull. Earthq. Eng. 11 (2013) 1797–1816. doi:10.1007/s10518-013-9437-4.

[37] ASTM, ASTM A416/A416M-05, Standard Specification for Steel Strand, Uncoated Seven-Wire for Prestressed Concrete, West Conshohocken, PA, USA, 2005.

[38] T.L. Bruce, M.R. Eatherton, Behavior of Post-Tensioning Strand Systems Subjected to Inelastic Cyclic Loading, J. Struct. Eng. 142 (2016) 04016067. doi:10.1061/(ASCE)ST.1943-541X.0001503.

[39] P. Sideris, A.J. Aref, A. Filiatrault, Effects of anchorage hardware on the cyclic tensile response of unbonded monostrands, PCI J. 59 (2014) 60–77. doi:10.15554/pcij.06012014.60.77.

[40] G.A. MacRae, C.R. Urmson, W.R. Walpole, P. Moss, K. Hyde, C. Clifton, Axial shortening of steel columns in buildings subjected to earthquakes, Bull. New Zeal. Soc. Earthq. Eng. 42 (2009) 275–287.

[41] R. Vargas, M. Bruneau, Analytical Response and Design of Buildings with Metallic Structural Fuses. I, J. Struct. Eng. 135 (2009) 386–93. doi:10.1061/(ASCE)0733-9445(2009)135:4(386).

[42] Y.-C. Lin, R. Sause, J.M. Ricles, Seismic Performance of a Large-Scale Steel Self-Centering Moment-Resisting Frame: MCE Hybrid Simulations and Quasi-Static Pushover Tests, J. Struct. Eng. 139 (2013) 1227–1236. doi:10.1061/(ASCE)ST.1943-541X.0000661.

[43] T.C. Steele, L.D.A. Wiebe, Collapse risk of controlled rocking steel braced frames with different post-tensioning and energy dissipation designs, Earthq. Eng. Struct. Dyn. (2017). doi:10.1002/eqe.2892.

[44] BS EN 1993-1-1, Eurocode 3: Design of steel structures - Part 1-1: General rules and rules for steel buildings, United Kingdom, 2009.

[45] BS EN 1993-1-8, Eurocode 3 : Design of steel structures — Part 1-8 : Design of joints, United Kingdom, 2010.

[46] L. Wiebe, C. Christopoulos, Performance-Based Seismic Design of Controlled Rocking Steel Braced Frames. I: Methodological Framework and Design of Base Rocking Joint, J. Struct. Eng. 141 (2015). doi:10.1061/(ASCE)ST.1943-541X.0001202.

[47] G. Vasdravellis, T.L. Karavasilis, B. Uy, Finite element models and cyclic behavior of self-centering steel post-tensioned connections with web hourglass pins, Eng. Struct. 52 (2013) 1–16. doi:http://dx.doi.org/10.1016/j.engstruct.2013.02.005.

[48] U. of C. Pacific Earthquake Engineering Research Center (PEER), OpenSees, (2015). http://opensees.berkeley.edu.

[49] M.H. Scott, G.L. Fenves, Plastic hinge integration methods for force–based beam-column elements, J. Struct. Eng. 132 (2006) 244–252.

[50] D.G. Lignos, H. Krawinkler, Deterioration Modeling of Steel Components in Support of Collapse Prediction of Steel Moment Frames under Earthquake Loading, J. Struct. Eng. 137 (2011) 1291–1302. doi:10.1061/(ASCE)ST.1943-541X.0000376.

[51] M. Hamidia, A. Filiatrault, A.J. Aref, Simplified seismic sidesway collapse analysis of frame buildings, Earthq. Eng. Struct. Dyn. 43 (2014) 429–448. doi:10.1002/eqe.2353.

[52] H. Krawinkler, Shear in Beam-Column Joints in Seismic Design of Frames, Eng. J. 15 (1978).

[53] C.C. Chou, K.C. Tsai, W.C. Yang, Self-centering steel connections with steel bars and a discontinuous composite slab, Earthq. Eng. Struct. Dyn. 38 (2009) 403–422. doi:10.1002/eqe.856.

[54] G. Vasdravellis, M. Baiguera, D. Al-Sammaraie, Robustness assessment of a steel self-centering moment-resisting frame under column loss, J. Constr. Steel Res. 141 (2018) 36–49. doi:10.1016/j.jcsr.2017.11.004.

[55] M. Bruneau, C.-M. Uang, R. Sabelli, Ductile design of steel structures, Second Edi, McGraw-Hill Education, 2011.

[56] P. Uriz, Towards Earthquake Resistant Design of Concentrically Braced Steel Structures, University of California, Berkeley, USA, 2005.

[57] VSL International Ltd, Post-tensioning, stay cables & construction methods, Prod. Broch. VSL STRAND POST-TENSIONING Syst. (2013). www.vsl.com.

[58] M. Baiguera, G. Vasdravellis, T.L. Karavasilis, Ultralow Cycle Fatigue Tests and Fracture Prediction Models for Duplex Stainless-Steel Devices of High Seismic Performance Braced Frames, J. Struct. Eng. 145 (2019) 04018230. doi:10.1061/(ASCE) ST.1943-541X.0002243.

[59] FEMA, Quantification of building seismic performance factors (FEMA P695) (ATC-63 Project), USA, 2009. https://www.fema.gov/media-library-data/20130726-1716-25045-9655/fema_p695.pdf.

[60] ASCE/SEI, Seismic rehabilitation of existing buildings (ASCE/SEI 41-06), U.S.A., 2007.

[61] L.T. Kibriya, C. Málaga-Chuquitaypea, M.M. Kashani, N.A. Alexander, Nonlinear dynamics of self-centring rocking steel frames using finite element models, Soil Dyn. Earthq. Eng. 1115 (2018) 826–37. doi:https://doi.org/10.1016/j.soildyn.2018.09.036.

[62] J. McCormick, H. Aburano, M. Ikenaga, M. Nakashima, Permissible Residual Deformation Levels for Building Structures Considering both Safety and Human Elements, in: 14th World Conf. Earthq. Eng. Oct. 12-17, China Earthquake Administration Ministry of Construction, Beijing, China, 2008.

[63] D. Vamvatsikos, C.A. Cornell, Incremental dynamic analysis, Earthq. Eng. Struct. Dyn. 31 (2002) 491–514. doi:10.1002/eqe.141.

[64] C.Y. Seo, T.L. Karavasilis, J.M. Ricles, R. Sause, Seismic performance and probabilistic collapse resistance assessment of steel moment resisting frames with fluid viscous dampers, Earthq. Eng. Struct. Dyn. 43 (2014) 2059–2216. doi:10.1002/eqe.2440.

[65] J.W. Baker, C.A. Cornell, Spectral shape, epsilon and record selection, Earthq. Eng. Struct. Dyn. 35 (2006) 1077–95. doi:10.1002/eqe.571.